Distribution Agreement

In presenting this thesis as a partial fulfillment of the requirements for a degree from Emory University, I hereby grant to Emory University and its agents the non-exclusive license to archive, make accessible, and display my thesis in whole or in part in all forms of media, now or hereafter know, including display on the World Wide Web. I understand that I may select some access restrictions as part of the online submission of this thesis. I retain all ownership rights to the copyright of the thesis. I also retain the right to use in future works (such as articles or books) all or part of this thesis.

William D. Dunn Jr. 20 March 2012

Radiogenomic Analysis of Clinically Relevant MRI Features in Glioblastoma Multiforme

by

William D. Dunn Jr.

David A. Gutman, MD, PhD

Neuroscience and Behavioral Biology

_____

David A. Gutman, MD, PhD

Adviser

_____

Patricia Marsteller, PhD

Committee Member

_____

Keith Easterling, PhD

Committee Member

_____

2012

Radiogenomic Analysis of Clinically Relevant MRI Features in Glioblastoma Multiforme

by

William D. Dunn Jr.

David A. Gutman MD, PhD

An abstract of
a thesis submitted to the Faculty of Emory College of Arts and Sciences
of Emory University in partial fulfillment
of the requirements of the degree of
Bachelor of Sciences with Honors

Neuroscience and Behavioral Biology

2012

Abstract

Radiogenomic Analysis of Clinically Relevant MRI Features in Glioblastoma Multiforme
By William D. Dunn Jr.

Background: Glioblastoma Multiforme (GBM) is a highly malignant form of brain cancer with one of the worst median survival times of all cancers. GBM tumors are characterized by several types of heterogeneity which ultimately lead to the failure of even the most intensive treatment regimens. Current research has uncovered diversity at genetic, epigenetic, and transcription levels of tumor cells, suggesting that an optimal standard of care should be tailored to individual patients harboring tumor cells with specific genomic aberrations.

Methods: In Part One of this study, we validate a novel semi-automated *in silico* volumetric image feature segmentation method and explore the potential prognostic power of several imaging features. In Part Two, we use both bottom-up and top-down approaches to correlate MR imaging features to several genomic aberrations of GBM.

Results: We find that our segmentation method agrees more with other volumetric techniques than with radiologists' scorings from qualitative standards and that several imaging features, notably percent necrosis (HR=1.862, P=0.01), are strongly correlated with survival. Bottom-up imaging feature / genomic correlations suggest MGMT promoter methylation status, but not EGFR or TP53 mutations or molecular subtype, is associated with certain imaging features. Top-down analyses using microarray data combined with bioinformatic software correlates anti-apoptosis, growth and proliferative, and cell death pathways with the percent necrosis imaging feature.

Conclusion: We have developed and verified a robust image feature measurement methodology for GBM tumors and show that it has statistical power to both predict survival as well as to implicate various molecular pathways with certain imaging features. Magnetic resonance imaging features have the potential to serve as non-invasive biomarkers for several clinically relevant molecular pathways.

Radiogenomic Analysis of Clinically Relevant MRI Features in Glioblastoma Multiforme

By

William D. Dunn Jr.

David A. Gutman, MD, PhD

Adviser

A thesis submitted to the Faculty of Emory College of Arts and Sciences
of Emory University in partial fulfillment
of the requirements of the degree of
Bachelor of Sciences with Honors

Neuroscience and Behavioral Biology

2012

Acknowledgements

I would like to thank first and foremost Dr. David Gutman, who has been my mentor and research advisor for the past two years, for his guidance and encouragement. I have learned so much in clinical research, computing, biomedical informatics, and healthcare in general that I would be in a much different place now had I not decided to join his lab.

In addition, I would like to thank the following who, without their help, this thesis would not have been possible:

Lee Cooper, PhD – For assistance in acquiring, normalizing, and organizing genetic expression data.

Doris Gao, PhD – For showing me there is so much more to survival analyses than simple linear regression in Excel.

Tarun Aurora, B.S. – For helping me with imaging feature annotations as well as with compiling patient imaging and gene expression data.

I would also like to thank my committee members for their time and insight: Dr. Easterling for his encouragement and guidance in helping me organize my writing and Dr. Marsteller for all of her invaluable support throughout my undergraduate career.

Table of Contents

Introduction

Glioblastoma Multiforme (GBM) is one of the most malignant forms of primary brain cancer and has a dismal median survival of only 14 months post diagnosis (Van Meir et al., 2010). GBMs are composed of highly proliferative and invasive anaplastic glial cells that typically originate in the white matter of the brain (Rees, et al., 1996). At the histological level, tumors are characterized by cellular pleomorphism, dense cellularity, variable mitotic activity, neovascularity, and psuedopalisading necrosis (White, et al., 2005). Besides the current standard of care involving gross total surgical resection, radiation therapy, and temozolomide chemotherapy, affected patients are left with few options. Despite surgical (Tonn & Stummer, 2008; Westphal et al., 2003), radiation (Stieber & Mehta, 2007), and chemotherapeutic (Norden et al., 2008) advances, relatively little progress has been made in the last 20 years in terms of overall survival (Mao, et al., 2012; Yamada et al., 1992).

One possible explanation for the lack of improvement may be that a blanket approach to treatment ignores the complex heterogeneity inherent in GBM. As "multiforme" implies, GBMs show heterogeneity both within an individual patient as well as between patients. Within an individual, the surrounding microglia, macrophages, extracellular matrix, and endothelial cells of the microenvironment cause natural selection pressures to increase diversity of proliferation rate, chromosomal abnormality, morphology, and even drug resistance of the individual cells (Bonavia, et al., 2011). Moreover, even when tumor cells have identical morphology, the underlying genetic expression can be markedly dissimilar (Vitucci, Hayes, & Miller, 2011). Between patients, GBMs differ in size (M. Y. Wang et al., 2011), location, chromosomal aberration patterns, genetic expression (Verhaak et al., 2010), and epigenetic modifications (Esteller et al., 2000). For example, despite high histological and clinical similarity between *de*

novo GBM tumors and secondary GBM tumors, the two types differ so markedly in their genetic mutation profiles that defining them as separate entities altogether has been considered (Maher et al., 2001). This complex heterogeneity implies that the optimal standard of care may need to be tailored to specific properties of the tumor.

The Cancer Genome Atlas (TCGA) project was designed in 2005 to comprehensively catalogue the various genome, epigenome, and transcriptome alterations that are involved in cancer origination and maintenance. TCGA houses both raw and normalized data from several "omic" platforms measuring DNA copy number, gene expression (via mRNA microarray analysis), DNA methylation, and nucleotide sequence aberrations of several hundred GBM tumors. Results from comprehensive TCGA studies both introduce novel alterations involved in tumorigenesis, such as amplifications in the AKT3 gene and deletions in NF1 and PARK2, as well as corroborate and extend previous literature describing the three core pathways in glioblastoma: RTK/RAS/PI(3)K, p53, and RB signaling pathways (Cancer, T., & Atlas, G. 2008) (Figure 1). TCGA research has identified points of deregulation in each of these pathways and their frequencies across patients. For instance, epidermal growth factor receptor (EGFR), which is involved in the RTK/PAS/PI(3)K pathway and drives proliferation and survival of tumor cells, is mutated or amplified in 45% of GBM patients. Tumor protein 53 (TP53), a tumor suppressor involved in the maintenance of proper apoptosis and senescence of tumor cells, is mutated or deleted in 35% of patients.

Furthermore, hierarchical clustering of aggregated genetic expression data from over 200 GBM patients has recently demonstrated that there are actually four subtypes of GBM tumors: classical, proneural, mesenchymal, and neural (Verhaak et al., 2010). Different subtypes are characterized by differences in genomic mutations, overall survival following diagnosis, age, and

even drug response. For example, patients with the proneural subtype respond significantly less to intensive temozolmide chemotherapy than patients with other subtypes of GBM. One explanation is that proneural tumors tend to show demethylation of the promoter of the O-6-methylguanine-DNA methyltransferase (MGMT) gene, which encodes a DNA repair enzyme involved in deacetylation. This demethylation increases the transcription of the enzyme which likely interferes with the DNA alkylation mechanism of temozolomide (Hegi et al., 2005). Thus, variability at the molecular level seems to be the norm, not the exception, of GBM related pathogenesis.

Since the underlying molecular pathways are the ultimate target of chemotherapeutic intervention, a better understanding of the potential pathways involved in tumorigenesis will ideally drive the selection of more individualized chemotherapeutic regimens and improve quality of care (Quant & Wen, 2010). For example, patients with proneural subtypes may respond better to drugs that target increased expression of platelet derived growth factor receptor (PDGFRα) than temozolomide. Others have proposed that altering chemotherapeutic interventions based on a patient's MGMT promoter methylation status could lead to longer survival (Stupp et al., 2005). Likewise, patients with EGFR mutations may be more likely to benefit from PI(3)K or PDK1 inhibitors and patients with TP53 mutations could be better candidates for CDK inhibitors (Cancer, T., & Atlas, G. 2008).

Magnetic Resonance Imaging (MRI) is routinely used in GBM clinical care and its role is currently limited to initially indicating abnormalities in the skull and to monitoring the tumor's response to therapy. While genomic screenings are becoming increasingly important in the characterization of tumors, complementary macroscopic properties of the tumor which reflect processes such as growth and infiltration also have significant effects on outcome and are

important to investigate. Since the sample that ultimately goes for ‘omics’ analysis only represents a small piece of the overall tumor, macro and micro environmental factors both need to be considered in order to have a complete understanding of the tumor.

Cortical GBM tumors often appear on MRI scans as indicated in Figure 2. Different MRI sequences provide differential contrast to highlight different tissues and imaging features that represent biological processes. T1 weighted, T2 weighted, and fluid attenuated inversion recovery (FLAIR) are commonly used sequences for static image properties. Besides contrast generated by the MRI itself, exogenous agents such as solutions of gadolinium (Gd) complexes, can be administered intravenously to highlight certain features. The imaging feature contrast enhancement refers to the increased signal in post Gd contrast T1 weighted scans and is a characteristic feature of high grade gliomas (Garzon et al., 2011). Contrast enhancement implicates several processes involved in pathogenesis, principally the disruption of the basement membrane of capillaries in the blood brain barrier and the alteration of the extra cellular matrix (ECM). These disruptions likely result from vascular endothelial growth factor (VEGF) mediated angiogenesis, a process critical for supplying neoplastic tissue with oxygen to meet its metabolic needs (Zagzag et al., 1989). Gadolinium based contrast agents leak out of the fenestrated neovasculature, bind to various proteins, and are easily visualized on MRI (Figure 2C). Edema, best visualized as increased signal intensity on FLAIR and T2 weighted images, reflects the swelling and accumulation of fluid in different tissues as a result of tumor infiltration (Zinn et al., 2011) (Figure 2A,B). Necrosis refers to the decreased signal intensity on T1 weighted images and represents prematurely killed cells, likely resulting from the high growth rate of glioblastoma depleting nutrients and blood supply of the inner cells (Raza et al., 2004) (Figure 2C).

MRI has also been a useful tool in understanding the molecular characteristics of brain tumors. At the DNA level, sequencing technology has allowed researchers to infer genetic correlations between germline mutations in tumor protein p53 gene and multifocal tumors (Kyritsis et al., 1994) and between IDH1 mutations and different levels of contrast enhancement (Carrillo et al., 2012). Expression microarrays are another useful technology and allow for the ability to interrogate the expression of tens of thousands of genes in a single experiment. For example, the amounts of VEGF and angiopoetin-2 expression have been correlated to levels of edema (Carlson et al., 2007). While elucidating the roles of specific genes is important in identifying individual molecular targets, gene expression microarrays can be also combined with bioinformatic analyses to understand the mechanisms and pathways that are involved with various imaging features. For example, Diehn *et al.* found that the imaging feature of mass effect (resulting from growing tumor pressing against other areas of the brain) was highly correlated to the genetic expression of genes involved in proliferation and cell-cycle progression (Diehn et al., 2008). Likewise, similar procedures were used to conclude that genes involved in blood brain barrier maintenance, hypoxia, angiogenesis, and extracellular matrix remodeling were significantly up-regulated in high contrast enhancing tumors compared to low contrast enhancing tumors (Pope et al., 2008).

The actual determinants of malignant potential and treatment response are dependent on the aberrations at the molecular level, which currently play a very limited role in the clinical settings (Colman et al., 2010) due to the financial cost, time, and required manpower to analyze and interpret large scale genomic data (George et al., 2011). Reported here is an attempt to assess the role that MRI technology could play as a cost effective biomarker to assist physicians with prognostic and diagnostic decisions. We believe that by correlating clinically relevant MRI

features to genomic aberrations, we can gain a better understanding of the molecular pathways of different GBM tumors. This study is divided into two parts.

In Part One, we validated our MRI feature segmentation and measurement methodology and investigated its prognostic value using data from 89 individuals. The technique used here is a novel semi-automated *in silico* measurement pipeline that measures various imaging features in continuous, volumetric variables. Because there is currently no "gold standard", this method was first validated based on how well the imaging feature measurements agreed with consensus measurements made by three board certified radiologists based on a non-quantitative standard (VASARI, see below). We also compared our measurements to those made by a collaborating group using a different quantitative imaging feature segmentation method. (Zinn et al., 2011). As further validation, we briefly investigated how well our method agreed with the literature in stratifying patients into high and low survival groups based on imaging features.

We next tested in depth whether any particular imaging feature was predictive of survival, controlling for known prognostic indicators such as the functional status of the patient at time of diagnosis (using the Karnofsky Performance Scale, KPS) (Krex et al., 2007), age (Curran et al., 1993), and gender (Tugcu et al., 2010). Several metrics derived from combinations of features were also tested because prior work has suggested that response to chemotherapy may depend on the ratios or relative amounts of imaging features (Najafi et al., 2012) and because other studies have determined that some features are not predictive of survival unless they are combined (Ellingson et al., 2011). Indeed research from our own lab has shown that patients with a high ratio of contrast enhancement to necrosis have lower survival, presumably because the high relative amount of contrast enhancement indicates a rapidly growing tumor (Gutman *et al*., in review). We also studied several imaging features in terms of percent of the total abnormal

volume to control for tumor size, which may be a significant prognostic factor (Hammoud et al., 1996).

Certain MR imaging features have been shown to have prognostic significance directly after surgery such as residual tumor volume and relative cerebral blood volume (rCBV) and are able to help doctors determine whether or not a patient should advance to radiation and chemotherapy (Saraswathy et al., 2009). Several preoperative MRI features, such as tumor volume, necrosis, contrast enhancement, and edema, have also been implicated in terms of overall survival, though these studies have led to several conflicting results (Table 1). Note the actual location of the tumor is also a potential prognostic variable, but due to conflicting results of previous studies, we did not analyze its influence in this report. Apart from small sample sizes, these disagreements likely arise from the types of methods used in most image feature / survival association studies to date. For one, many results are based on the image feature measurements of only a single two dimensional image. The central axial slice is usually chosen because it typically has the least partial volumes and is thus considered to reflect the most accurate tissue features (Soltanian-Zadeh et al., 1998). Moreover, most of these studies involved trained neuroradiologists measuring imaging features in categorical variables. For example, in their study of survival and necrosis, Ekici *et al.* quantified the level of necrosis into four quartiles (0-III) (Ekici et al., 2011). In a previous study in which our lab was involved, images from a subset of the patients used in the current study were scored by three board certified neuroradiologists according to the VASARI (Visually Accessible Rembrandt Images) standard. VASARI consists of 30 measurement features with specific guidelines on how to score each (i.e. 0-5%, 6-33%, 34-67%, or 68-95% or >95% contrast enhancing) and it is designed to allow for accurate and reproducible MR image scoring (Appendix Figure 1). A number of factors make

this type of assessment especially unreliable. The greatest challenge may be the lack of a true gold standard to measure our results against, but other challenges arise from the inherent probabilistic nature of MRI images, the differences in what different radiologists consider to be an imaging feature, and the fact that visualizing certain imaging features depends on arbitrarily-set relative pixel intensities. Our technique, which actually counts the individual pixels, allows the direct measurement of MRI features. We believe that this increased precision will lead to more accurate and reproducible results.

In Part Two, we attempted to connect these imaging features to events occurring at the molecular level. We began with a bottom up approach by correlating the measured imaging features with pre-established genomic characteristics of our 89 patients. The TCGA database contains results from sequencing analyses determining the mutation status of several oncogenes and tumor suppressors often mutated in cancer, such as TP53 and EGFR. We wanted to know if certain imaging features could give us insight into the mutation status of the respective tumor. For each of these two genes, we compared the level of each of our features between both mutated tumors and wild type tumors. We used a similar methodology to determine if imaging features could be correlated to methylation status of the MGMT promoter or to the molecular subtype of the underlying tumor. If we were able to find mappings between specific imaging features and mutation status, MGMT promoter hypermethylation, or molecular subtype, it would strengthen our hypothesis that GBM tumors with different genomic fingerprints appear differently at the macroscopic MRI level.

Furthermore, we used a top down approach with the aid of gene expression microarray data to explore additional pathways and genomic aberrations associated with specific imaging features. We focused on the one imaging feature that we found to be the most predictive of

survival, percent necrosis. For this analysis, we used Significance Analysis of Microarray (SAM) software to identify genes that are differentially expressed between patients with high and low levels of percent necrosis. Based on the results of this analysis, the genes identified were then subjected to pathway analysis and key pathways involved in the relevant imaging feature were identified.

Materials and Methods

Patient Population

MRI sets from 129 patients from various institutions, including Emory University, were downloaded from the Cancer Imaging archive (TCIA). Image sets containing both FLAIR and post Gd T1 weighted images were downloaded in DICOM-format and were individually reviewed before feature segmentation (see below) to confirm pre-surgical and treatment-naive status as well as to exclude images of exceptionally poor quality. As the patients had been previously de-identified by the TCGA and are available for public download, no Institutional Review Board approval was required.

Image segmentation, volumetric measurement, and feature classification

Brain tumor regions were broadly identified as regions showing signal enhancement (e.g. increased brightness) following gadolinium contrast administration. Cases where the tumor margin was not readily identifiable were flagged for secondary review by a physician. For post Gd T1 images, binary masks were manually drawn over the tumor and the region it surrounds using a segmentation tool in Velocity AI (Figure 3A). Velocity AI (Atlanta, GA) is a software platform developed at Emory for radiation therapy treatment and image fusion, and is ideally suited for the markup/masking and visualization of MRI images.

Similarly, for FLAIR-based sequences, FLAIR "envelopes" were drawn in an analogous manner to the post-Gd T1 images (Figure 3B). The total volume marked up on the FLAIR sequence included bright areas indicative of edema/swelling as well as other regions that showed signal abnormalities (Pavlisa et al., 2009). Because we were interested in the FLAIR signal as an estimation of overall tumor involvement, we limited the FLAIR segmentations to the ipsilateral side of the tumor and did not include the signal that may be due to ventricular spread.

Following initial tumor markup, the masks were exported from Velocity AI as DICOM-RT objects. These image markups were subsequently converted to NIFTI and PNG formats to allow further visualization and segmentation. As a secondary quality check, a custom visualization platform was developed as part of a larger project in our lab ("TumorView", Figure 4) which allowed for rapid screening of the image volumes that were analyzed for this study. This tool helped to eliminate post surgical image sets (and hence not amenable to estimation of pre-surgical tumor volume) and images of particularly poor quality, as well as to ensure that the masks and accompanying images were overlaid and exported properly.

Contrast enhancing and necrotic volumes were calculated from the masked region on post Gd T1 images using FAST (FMRIB Automated Segmentation Tool, http://www.fmrib.ox.ac.uk/fsl/fast4/index.html). Briefly, for the masks drawn on the post Gd T1 images, which included both contrast enhancing and necrotic regions, k means clustering identified two clusters based on relative pixel intensity. This resulted in a binary classification of tumor into either bright (contrast enhancing) or dark (necrotic) regions (Figure 5). This voxel-based measure could then be directly converted into volumetric measures by multiplying the number of bright or dark voxels by the voxel size in mm^3.

For subsequent analysis, we defined the *total tumor volume* as the sum of the necrotic and contrast enhancing volumes. For the FLAIR images, the entire "envelope" volume is referred to as the *total abnormal volume* (Figure 3B). The edema volume refers to the area resulting from the subtraction of total tumor volume from total abnormal volume. Percent necrosis, percent edema, or percent contrast enhancement refers to the necrotic, edematous, or contrast enhancing volume, respectively, divided by the total abnormal volume.

Semi-automated *in silico* measurement technique validation

To assess the accuracy of our tumor markups, we identified a subset of patients that have been used in a previous study involving the TCGA GBM data set. Working with collaborators at the National Cancer Institute (NCI), we obtained qualitative assessments of neuroimaging features for these patients. These assessments were made by three board certified radiologists who estimated the necrotic, edematous, and contrast enhancing volumes of the tumor based on the VASARI standard. A consensus rating was generated for each patient, and we compared these ratings to our continuous volumetric measurements. Specifically, our necrosis, contrast enhancement, and edema volume measurements from 59 overlapping patients were transformed into the appropriate VASARI features (percent necrosis, percent contrast enhancing, and percent edema) and we measured the Cohen's κ metric of agreement (Cohen, 1960) for how often our volumetric measurements fell within the range of the consensus ratings for each variable.

For additional validation, we obtained an additional data set from our collaborator at Massachusetts General Hospital (R. Colen, personal communication, and (Zinn et al., 2011)). This data set also consisted of continuous volumetric assessments of the tumor into necrosis, contrast enhancement, and edematous regions, but was generated using a completely different platform (3d-SLICER, MGH, http://www.slicer.org/). In addition, a board-certified

neuroradiologist (R. Colen) manually performed the actual image segmentations of necrotic and contrast enhancement regions. As described above, the volumes in this dataset were transformed into the applicable features of the VASARI standard and were compared to the consensus ratings for the 59 patients with overlapping data.

The concordance between each of the two volumetric data sets (Zinn *et al.*/Gutman *et al.*) with the neuroradiologists' ratings according to the VASARI standard was also compared. Percent agreement indicated the frequency that our measurements or those made by (Zinn et al., 2011) fell within the VASARI ranges divided by the number of patients with overlapping data (n=59). To determine if one of the two volumetric data sets agreed more with the radiologists' scores than the other, our percent agreement for each feature was compared with that of Zinn *et al.* using a pooled two proportion z test.

We also used a metric from Gutman *et al.* (in review) to determine how well our measurements and those from Zinn *et al.* agreed with previous studies implicating necrosis with lower overall survival (Table 1). Briefly, the levels of necrosis in patients living more than twelve months are compared to those living less than twelve months. Thus, significant differences in levels of necrosis between these two groups would reflect more agreement with previous literature.

Survival analysis

To identify imaging features of potential prognostic value for GBM patients, hazard ratios were computed from both univariate and multivariate Cox regression models (H. Wang et al., 2008). First, to explore the effects of individual imaging features and patient variables on survival, univariate models were used to calculate the hazard ratio for each variable. The

differences in prognostic power were assessed by examining the relative hazard ratio and P value for each variable.

Forward variable selection was used to build a multivariate model consisting of significant univariate patient and imaging feature variables. For our study, only the significant univariate patient variables and the significant imaging feature variable with the highest univariate hazard ratio were used.

To obtain manageable hazard ratios, all independent variables were log-transformed. If the patient was still alive at the end of the study, his/her status of survival was considered to be *right-censored* and the days to last follow-up were used as the survival time (10/89 patients). Kaplan-Meier survival curves were also constructed to visualize survival differences between patients dichotomized in terms of having levels of percent necrosis above and below the median: (19.5%).

Radiogenomic correlation

For the bottom up study, correlations were made between imaging features and molecular features already available through TCGA. Mutation statuses of EGRF and TP53 were previously inferred from Sanger sequencing as described elsewhere (Cancer, T., & Atlas, G. 2008). MGMT promoter methylation status was previously identified in level three data downloaded from the TCGA data portal as “methylated” or “unmethylated” according to the method used by (Grasbon-Frodl et al., 2007). GBM molecular subtypes were previously determined by consensus clustering (Verhaak et al., 2010). Independent samples t tests were used to compare the average levels of each of the 17 imaging features (Table 3A) between patients with or without EGFR or TP53 mutations as well as between patients with or without MGMT promoter hypermethylation. Unless indicated otherwise by Levene’s test for equality of variance, all t tests were conducted

on the assumption of equal variance. One way between subjects analyses of variance (ANOVAs) were used to compare the level of each imaging feature between the four different molecular subtypes.

For the top down analyses, genetic expression was measured using an Affymetrix Human Genome U133A chip, which measures approximately 22,000 probes, corresponding to approximately 14,000 genes. Level two expression data was downloaded from the TCGA data repository and probe expression was normalized against housekeeping genes and eliminated if expression was not significant as performed in a previous study (Cooper et al., 2012).

To identify genes correlated with percent necrosis, patients were divided into thirds in terms of percent necrosis as performed elsewhere (Zinn et al., 2011). Expression data from the top third was compared to that of the bottom third using SAM (Statistical Analysis of Microarray), an Excel plug-in developed at Stanford (http://www-stat.stanford.edu/~tibs/SAM/). An advantage of SAM is that it uses permutation testing to estimate false discovery rates (FDR) which helps eliminate those genes whose differential expression is likely due to chance (Tusher et al., 2001)**.** A visual representation of a SAM analysis output is demonstrated in Appendix Figure 2. For our study, 500 permutations were used in each analysis. To account for the large variability in microarray expression values between subjects and to control for the effect of outliers, the Wilcoxon signed ranks tests option was used in lieu of the standard t test option to compare expression of each gene between high and low percent necrosis groups.

Similar tests were computed for individual molecular subtypes and a set of genes that were consistently differentially expressed between high and low levels of percent necrosis independent of molecular subtype was chosen. To ensure the significance of our gene list, only genes with false discovery rates below 40% were considered for the analysis.

Molecular Pathway Analysis

To understand the molecular pathways associated with an image feature, the above gene set was analyzed through Ingenuity Pathway Analysis (IPA, http://www.ingenuity.com). The associations of our genes with relevant networks, well-characterized canonical pathways, and pathological pathways were investigated.

Statistics

All independent t tests, one way between subject analyses of variance (ANOVAs), and Kaplan Meier survival curves were computed using Graphpad Prism (La Jolla, CA). SPSS (IBM Corporation, Armonk, NY) was used to compute Tukey's post hoc tests for one way ANOVAS and both univariate and multivariate Cox regression models. Unless otherwise specified, P values less than 0.05 were considered significant.

Results

89 of the original 129 patients had images that were amenable to complete necrosis, contrast enhancement, and edema measurements and were used in this study (57/89 male). Patient age ranged from 14 to 84 years with a median age of 60 (Figure 6). Median survival from date of diagnosis was 399 days, consistent with previous reports (Krex et al., 2007). Sample statistics of several image feature volumes across these 89 patients are listed in Table 2.

Part One – Semi-automated *in silico* feature measurement validation

Agreement with neuroradiologists' scores based on VASARI reference data.

The measurements made from our methodology and those made by board certified neuroradiologists agreed fairly in terms of percent contrast enhancement and percent necrosis

(Cohen's κ=0.238 and 0.304 respectively), but agreed poorly in regards to percent edema (Cohen's κ=-0.07) (Landis & Koch, 1977). For comparison, the Cohen's κ between Zinn *et al.* and the consensus VASARI scores for percent contrast enhancement, percent necrosis, and percent edema was 0.183, 0.198, and -1.24 respectively. Percent agreement with VASARI of both our measurements and those from Zinn *et al.* is plotted in Figure 7. For each imaging feature, there was no significant different between our data and that from Zinn *et al.* in terms of agreement with the neuroradiologists ratings: percent edema: $Z(59) = 0.604$, $P=0.546$ (two tailed); percent contrast enhancement: $Z(59) = 0.828$, $P=0.408$ (two tailed); percent necrosis: $Z(59) = 1.848$, $P=0.065$ (two tailed).

Agreement with Zinn *et al.*

Our measurements were also directly compared to those of Zinn *et al*. for the 70 patients represented in both data sets. Patient TCGA-06-0162 was removed from the analysis due to diffusely contrasting tumor (Figure 8). Significant Pearson correlations between Zinn *et al.* and Gutman *et al.* were obtained for each of five general imaging features. The highest correlations were seen in total abnormal volume ($r(70)=0.949$, $P<0.0001$), total tumor volume ($r(70)=0.944$, $P<0.0001$), and edema volumes ($r(70)=0.928$, $P<0.0001$). The lowest correlations were seen in contrast enhancing volume ($r(70)=0.770$, $P<0.0001$) and necrotic volume $r(70)= 0.612$, $P<0.0001$) (Fig 9).

The measurements from our data showed a much stronger significance in the difference between the levels of necrosis in patients surviving more than a year and patients surviving less than a year ($t(69)=3.43$, $P=0.0006$) than the difference using data from Zinn *et al.* ($t(69)=2.087$, $P=0.0212$) (Figure 10).

Imaging Features as Predictors of Survival

To identify imaging features of potential prognostic value for GBM patients, univariate analyses of each variable were performed in regards to overall survival time. Six imaging feature variables and one patient variable showed significant prognostic value and are indicated in Table 3A. Of particular interest, the ratio of necrotic volume over total abnormal volume (percent necrosis) appeared to have the highest significant effect on survival (HR=1.862, *P*=0.01). Patients with lower Karnofsky Performance Scale (KPS) scores also appeared to have shorter overall survival times (HR=1.473, *P*=0.046).

Percent necrosis and KPS variables were then used to build the multivariate Cox regression model shown in Table 3B. The results of the multivariate analysis showed that only percent necrosis was a significant prognostic factor in overall survival (HR = 1.713, *P*=0.03). Kaplan Meier survival curves for low and high levels of percent necrosis also showed significant separation (*P*=0.0209, log-rank test) (Figure 11).

For the subsequent microarray analysis, we focused on global changes in gene expression related to different levels of the percent necrosis imaging feature as this was the imaging feature most predictive of survival in our analysis.

The levels of necrosis did not differ as a function of age (one way ANOVA $F(2,86)=1.133$, $P=0.327$) (Figure 12A) or as a function of gender ($t(87)=0.236$, $P=0.814$) (Figure 12B). However, a one way between subjects ANOVA showed a significant effect of KPS score on percent necrosis ($F(2,66)=3.293$, $P=0.0433$, $\eta^2 = 0.091$). Post hoc analysis (Tukey's HSD) revealed that the mean percent necrosis of patients with KPS of 60 ($\bar{x} = 30.6$, SD = 13.51) was significantly greater than patients with KPS of 100 ($\bar{x} = 19.77$, SD = 11.6, $P=0.043$) (Figure 12C).

Part Two – Genomic correlates to MR imaging features

Bottom-Up Analyses

For patients with complete data, 14 out of 62 (22.6%) and 9 out of 62 (14.5%) patients had TP53 mutations and EGFR mutations respectively. Independent samples t tests showed no significant difference in the level of any of the 17 imaging features as a function of mutation status (Tables 4 and 5). A non-significant trend suggested that patients with TP53 mutations where characterized by smaller total abnormal volumes than patients without the mutation ($t(83)=1.475$, $P=0.144$).

For patients with complete data, 10 out of 51 (19.6%) patients had hypermethylated MGMT promoters. Patients with hypermethylated MGMT promoters tended to have higher contrast enhancement / total tumor ratios ($t(49)=2.932$, $P=0.005$) and contrast enhancement / necrosis ratios ($t(49) = 2.969$, $P=0.005$) (Table 6) (Figure 13).

Lastly, at the transcriptome level, the levels of each imaging feature in Table 3 were compared between the four molecular subtypes of GBM (20/85 proneural, 30/85 mesenchymal, 21/85 classical, 14/85 neural). A one-way between subjects ANOVA for each imaging feature failed to show any statistical significance between molecular subtypes of GBM (Table 7). The effect of molecular subtype on five general imaging features is illustrated in Figure 14.

Top: Down analyses: Imaging/Microarray Analyses

The results of our initial two-class non-parametric SAM analysis showed 1049 genes up-regulated between tumors with high and low percent necrosis below a false discovery rate of 30%. As we were originally interested in the genetic expression patterns for the necrosis imaging feature independent of molecular subtype, we next performed separate analyses for each of the four molecular subtypes of GBM in hopes of finding a consistent set of differentially expressed

genes between high and low necrosis groups. However, due to the inability to find a consistent set of genes at reasonable false discovery rates, we randomly divided our total group into a Discovery group and Validation group, again compared the genes differentially expressed between the top and bottom thirds of percent necrosis patients, and identified overlapping genes in both groups according to the method performed Zinn et al. (2011). 118 genes were consistently differentially expressed between these two groups at a false discovery rate below 40%.

Bioinformatic Analysis of selected genes associated with percent necrosis

We further analyzed the 118 genes whose expression was consistently correlated to percent necrosis using Ingenuity Pathway Analysis (IPA). The top associated molecular networks were cellular function and maintenance, cellular movement, hematological system development and function (59 genes), cancer, hematological disease, lipid metabolism (39 genes), cell to cell signaling, cellular growth and proliferation, connective tissue development and function (33 genes), and cell cycle, cell morphology, cellular growth and proliferation (17 genes). Figure 15 shows the involvement of several of the necrosis-associated genes within a subset of the growth and proliferation network.

Next, we analyzed the associated pathological pathways that were enriched in our gene set. Results show that significant pathways were hypoxia inducible factor signaling (P=0.0000643), anti apoptosis (P=0.0159), cell cycle: G2/M DNA damage checkpoint regulation (P=0.0341), and mitochondrial dysfunction (P=0.0501) (Figure 16). Table 8 shows the significance and genes associated with each of these pathways.

Finally, we analyzed the well established canonical pathways in which our genes were involved. Results showed that the top canonical pathways were EIF2 Signaling (P=2.08x10^{-06}),

Regulation of eIF4 and p70S6K signaling (P=2.84x10^{-04}), cardiac hypertrophy signaling (P=3.92x10^{-04}), systemic lupus erythematosus signaling (P=3.92x10^{-04}), and CREB signaling in neurons (P=3.78x10^{-03}). The P values in IPA estimate the likelihood that the association between our gene set and the respective pathways was due to random chance.

Discussion

In this study, we present a methodolgy to systematically and accurately analyze genomic correlations to MR imaging features in glioblastoma multiforme. In Part One, we showed that the results of our feature extraction measurements agreed more with other volumetric segmentation techniques than with the scorings made by radiologists according to the VASARI standard. This suggests that the visual estimations performed by neuroradiologists are likely inexact and not particularly sensitive. This is most likely due to the fact that using only one axial slice fails to give a complete representation of the tumor. In fact, during the segmentation process, we noticed that the relative amounts of contrast enhancement varied from slice to slice. For example, slices near the top and bottom of the tumor (representing the surface) often showed more contrast enhancement than those in the middle, a pattern not taken into account with a single 2D image.

While our volummetric assessment of tumor features is relatively consistent with those of Zinn *et al.,* one key difference is worth highlighting. In our methodology, only two markups are generated: an envelope covering the total abnormal signal in the FLAIR image and a mask covering the total tumor volume in the post Gd T1 images. Within the post Gd images, the total tumor volume consisted of interdigitated “necrosis” and “contrast enhancing” regions which FAST automatically separated. In contrast, the method used by Zinn *et al.* involved the manual segmentation of the region within the total tumor volume, which, besides being tedious and time-

consuming, can be highly subjective. Thus, the inherent differences in our volumetric methods could explain why there is more disagreement in contrast enhancing and necrotic volumes than in total tumor volume. Since a true gold standard does not exist, we determined which method was more "accurate", by how well it stratified short survivers and long survivers in terms of necrosis, a feature commonly implicated in the literature as having strong prognostic value. The results displayed in Figure 10 provide additional validation of our data set, as it suggests our measurements are not only consistent with past literature, but are as good if not better than the Zinn *et al.* dataset in predicting outcome.

Our edema measurments and those of Zinn *et al.* (2011) showed noticabely little agreement to the radiologists' scorings. This may be due to the fact that our definition of edema was based on the total abnormal volume, which contains both edema and other regions such as non-enhancing tumor (Carrillo et al., 2012; Kelly et al., 1987; Prastawa et al., 2005). As expected, when we did not agree with the VASARI standard, we over estimated the edema volume 98% of the time (data not shown). While there are several radiologist-based imaging standards other than VASARI (Therasse et al., 2000; Macdonald et al., 1990), there is not yet a volumetric, *in silico* based standard to objectively measure GBM imaging features that is routinily used in the clinic. We have shown that our method has statistically significant prognostic predictive power and we hope that our results will demonstrate that an objective, volumetric-based feature measurement pipeline is easy to implement and has the potential to provide meaningful guidence in prognostic and diagnostic decisions.

After having established the validity of our image segmentation technique, Part Two of this study focused on identifying associations between imaging features and genomic aberrations. In the first part of Part Two, we used a bottom up approach to correlate imaging

features to previously established genetic, epigenetic, and transcriptional characteristics of GBM tumors. We found that MGMT promoter methylation, but not EGFR mutations, TP53 mutations, or molecular subtype, was associated with several imaging features. Determination of MGMT methylation status is an important factor in estimating response to chemotherapy, but it is difficult to measure without taking large samples of tissue, usually only available from a biopsy or an tumor resection (Drabycz et al., 2010). Several studies have shown an association with MGMT promoter methylation and certain imaging features such as tumor location and ring enhancement patterns (Eoli et al., 2007). Future research could determine if a model could be built from combined imaging features to reliably predict the MGMT promoter methylation status of an individual before their initial surgical resection.

We were surprised that none of our 17 imaging features showed significant differences from each other across the molecular subtypes. Preliminary data from pilot studies with smaller sample sizes suggested at a borderline significance that the proneural subtype was characterized by less contrast enhancement compared to the other three subtypes. However, we did not find this trend in the current study (one way ANOVA: F (3, 63) = 7.13, P=0.548), suggesting that pathways other than those which differentiate molecular subtypes may be associated with various MRI features. To explore these pathways, a top-down approach was undertaken with the help of genetic expression microarray data.

In our microarray analysis, we were unable to find a consistent set of differentially expressed genes between high and low percent necrosis tumors across the four molecular subtypes of GBM. This may be due to the small sample sizes of the resepective subgroups compounded by the already decreased transcriptional activity of tumors with a high proportion of

dead cells. We therefore compared the differential expression between high and low necrosis using a discovery and validation set according to Zinn *et al.* (2011).

We decided to study the percent necrosis imaging feature for several reasons. For one, necrosis is consistently implicated throughout the literature as a poor prognostic indicator for a wide range of cancers (Fisher et al., 1978; Frank et al., 2002; Swinson et al., 2002). In regards to GBMs, necrosis is a strong prognostic MR imaging feature even when age, KPS, and gender is controlled for (Barker et al., 1996) and is often a defining hallmark at the histological level that differentiates GBM from lower grade gliomas (Louis et al., 2007). We also note that higher necrosis is associated with lower KPS scores and thus could influence overall patient health as well. Importantly, necrosis had historically been thought to be removed only by surgical measures, but recent research has demonstrated that it can actually be decreased chemotheraputically in patients with certain MRI features undergoing certain treatment regimens (Najafi et al., 2012). This suggests that it is possible to reduce necrosis by targeting pathways implicated in the phenotype. However, relatively little literature is available on the molecular pathways behind necrogenesis in regards to glioblastomas (Raza et al., 2004).

Apoptosis refers to the natural, programmed cell death that 99% of the cells in our bodies will undergo during our lifetimes. It is the orderly process that is defined by tightly regulated caspase-depdendent pathways and involves cooperation with the immune system to facilitate engulfment and to produce the least amount of immune disruption as possible. Necrosis, on the other hand, refers to unprgrammed cell death and is characterized by cytoplasmic swelling, plasma membrane rupture, organelle breakdown, and proinflammatory spilling of cellular contents into the surrounding tissue (Denecker et al., 2001). An important observation is that apoptosis and necrosis are the two possible pathways that a dying cell can take and which

pathway occurs depends on several factors such as intracellular ATP concentration (Lemasters, 1999). Therefore, one way to decrease necrosis in GBM could be to restore proper apoptotic pathways.

As expected, pathway analysis results demonstrated that several of our necrosis-related genes were involved in hypoxia, notably several eukaryotic initiation factor 2 subunits. Hypoxic situations and mitochondrial damage have been shown to lead to the phosphorylation of certain subunits of EIF2B and the inhibition of cellular protein synthesis (Lou et al., 2010). However, there is limited literature describing its role in tumorgenesis. Bioinformatic results also implicated several anti-apoptotic genes in our gene set. One potential anti-apoptotic target gene is baculoviral inhibitor of apoptosis (IAP) repeat-containing protein 7 (BIRC7), also referred to as livin, whose up-regulated expression has been reported in several cancers (Vucic et al., 2000) and is associated with lower overall survival in neuroblastoma due to its ability to attenuate apoptotic stimuli of chemotherapeutic agents (Kim et al., 2005).

It would also be expected that many of our necrosis-related genes would be involved in mitochondria dysfunction, as mitochondria play intricate roles in apoptosis. In order for cells to die in a controlled manner, the mitochondria undergoes a mitochondrial permeability transition (MPT) which is characterized by an increase in permeability to solutes with a simultaneous controlled release of proapoptotic proteins such as cytochrome c and various procaspases (Denecker et al., 2001). As mitochondrial integrity fails, apoptosis pathways are disrupted and cell death pathways shift to favor necrosis.

The top molecular networks enriched in our necrosis-associated genes involved cellular growth and proliferation, cell signaling, and connective tissue development and function (33 genes). Complementary studies in our lab investigating the expression patterns of patients with

increased levels of contrast enhancement, a feature which reflects the infiltration and angiogenesis of high-grade gliomas, have also implicated several of these pathways. It may seem counter-intuitive at first that pathways involved in new cell growth would be associated with tumors exhibiting marked patterns of cell death. However, a review of recent literature suggests the continuity between the two events and paints a picture of contrast enhancement and necrosis being two different sides of the same coin.

As tumor cells are stimulated to grow and proliferate uncontrollably, they release signals such as TNFα and NFκB, which are necessary for the coagulation required to stabilize neovasculature and ECM (Raza et al., 2004). This coagulation, combined with intravascular thrombosis resulting from high cellular density, is thought to strangle nutrient and energy sources and eventually lead to hypoxia (Brat & Van Meir, 2004). Hypoxic situations, in turn, cause interference with ligand-receptor interactions in the apoptosis pathway and shifts the death pathway to favor necrosis (Raza et al., 2004). Hypoxia also induces hypoxia inducible factors (HIFs) which, among other things, increase the transcription of vascular endothelial growth factor (VEGF) (Liu et al., 1995), leading back to angiogenesis, invasion, activation, and proliferation at the beginning of the cycle (Figure 17). This connection may explain both the high malignancy of highly necrotic tumors as well as the fact that the microvascular hyperplasia edges of necrosis, termed pseudopalisading necrosis, are the highest growing parts of the tumor (Brat & Van Meir, 2004) (Appendix Figure 3). Likewise, a high correlation between our contrast enhancement and necrotic volumes (Pearson $r(70) = 0.921$, $p<0.0001$, Appendix Figure 4) as well as studies that suggest that anti-VEGF therapies decrease necrosis preferentially (Pope et al., 2006) support this relation between necrosis and contrast enhancement. While the traditional method of measuring chemotherapeutic response rate is to monitor changes in contrast

enhancement (Shirai et al., 2012), this assessment fails to take into account important aspects of tumorgenesis. Our work corroborates the idea that in order to more fully understand the biology behind GBM, an understanding of contrast enhancement, as well as its complementary necrotic pathways, is required.

A word about the ethical implications of treatment of brain tumors

The decision of how to best treat GBM tumors is by no means a simple task. Doctors and family members are often faced with the difficult dilemma of weighing the costs of hundreds of thousands of dollars and tremendous setbacks in the quality of life from strong chemotherapeutic drugs and open craniotomy surgeries (sometimes multiple) and the benefits of prolonged survival.

Due to the aggressive nature and heterogeneity intrinsic amoung GBM tumors, the standard of care may lead to very different outcomes in relatively similar patients. This makes the decision more difficult and the obscruity of the situation allows doctors to perform procedures that would have been too risky to do otherwise, putting patients in compromised positions (Whittle & Gregor, 1991).

There are several factors that doctors currently use to stratify patients into survival groups to assist in decision making such as age, Karnofsky Performance Scale, and post-surgical residual tumor volume (Park et al., 2010). Our results have confirmed other studies suggesting that MRI may also be a useful tool to be used in the equation to guide decision-makers to the most practical ways of treating highly malignant neoplasms and lead to the longest period of high quality of life for GBM patients.

Limitations and future directions

Despite our increased precision by using two groups of patients and incorporating false discovery rates into our microarray analysis, it is important to note that our results may be confounded by issues inherent in DNA microarray analysis, such as the "multiple hypothesis caveat", which refers to the statistical probability that with so many genes, we would expect to see some genes to show significance by chance alone (Pope et al., 2008). Moreover, simply measuring mRNA levels only gives us a snapshot of the biological events between gene and protein. Future experiments involving western blots or immunohistochemical staining to measure protein amounts will be required to confirm our findings.

As another limitation, the tumor samples included in the TCGA studies were obtained from several different institutions, including Emory University, which did not record the time between initial sample collection at surgery and RNA processing or the location of the tumor from where the sample was taken. RNA is extremely sensitive and quickly degrades at room temperature (Strand et al., 2007), thus variable lengths of time between resection and snap freezing could obfuscate the interpretation of our results. Moreover, while limited studies have resulted in different conclusions about whether the microenvironment of the tumor affects genetic expression patterns (Hobbs et al., 2003) (Liang et al., 2005), it is likely that differences between necrotic regions and contrast enhancing regions do in fact influence gene expression and thus the location from where the tumor was taken could also influence the interpretation of our results. Current work in our lab is identifying the influence of tumor microenvironment on gene expression.

Conclusion

In Part One, we validated a novel semi-automated *in silico* segmentation and measurement method. This technique has the potential to be easily implemented in healthcare institutions and used by people with appropriate training. The approach involves measuring volumetric MR imaging features in continuous variables and offers more precision and reproducibility than typical measurement standards involving categorical variables.

In Part Two, we used both bottom-up and top-down approaches to implicate several molecular events with various imaging features. Our bottom-up results suggest that MGMT promoter methylation status is strongly associated with several imaging features. We chose to investigate the imaging feature percent necrosis in depth because of its strong relation to survival and the relative lack of literature examining its pathways. Results from bioinformatics analyses suggest several important pathological mechanisms and networks related to necrosis, such as hypoxia and anti-apoptosis, and identified several potential chemotherapeutic target genes. Lastly, our bioinformatic results and correlations between our image features corroborate the inseparability of contrast enhancement (angiogenesis, proliferation) and necrosis and the theme that one feature cannot be targeted without considering the other.

In summary, the goal of our project was to determine whether MRI features have the potential to be used in a clinical setting to assist with prognostic or diagnostic decision making and ultimately lead to more personalized therapies to improve the current standard of care for GBM. In the optimal setting, a doctor would volumetrically analyze an MRI feature, gain insight into the predominant oncologic molecular pathways involved in that tumor, and be better able to prescribe specific drugs for which that patient would likely be a good candidate. We hope that our findings will contribute to this ideal becoming a reality.

References

Barker, F. G., 2nd, Davis, R. L., Chang, S. M., & Prados, M. D. (1996). Necrosis as a prognostic factor in glioblastoma multiforme. *Cancer, 77*(6), 1161-1166.

Bonavia, R., Inda, M. M., Cavenee, W. K., & Furnari, F. B. (2011). Heterogeneity maintenance in glioblastoma: a social network. *Cancer Res, 71*(12), 4055-4060. doi: 10.1158/0008-5472.CAN-11-0153

Brat, D. J., & Van Meir, E. G. (2004). Vaso-occlusive and prothrombotic mechanisms associated with tumor hypoxia, necrosis, and accelerated growth in glioblastoma. *Lab Invest, 84*(4), 397-405. doi: 10.1038/labinvest.3700070

Cancer, T., & Atlas, G. (2008). Comprehensive genomic characterization defines human glioblastoma genes and core pathways. *Nature*, *455*(7216), 1061-8. doi: 10.1038/nature07385

Carlson, M. R. J., Pope, W. B., Horvath, S., Braunstein, J. G., Nghiemphu, P., Tso, C.-L., . . . Cloughesy, T. F. (2007). Relationship between Survival and Edema in Malignant Gliomas: Role of Vascular Endothelial Growth Factor and Neuronal Pentraxin 2. *Clinical Cancer Research, 13*(9), 2592-2598. doi: 10.1158/1078-0432.ccr-06-2772

Carrillo, J. A., Lai, A., Nghiemphu, P. L., Kim, H. J., Phillips, H. S., Kharbanda, S., . . . Pope, W. B. (2012). Relationship between Tumor Enhancement, Edema, IDH1 Mutational Status, MGMT Promoter Methylation, and Survival in Glioblastoma. *American Journal of Neuroradiology*. doi: 10.3174/ajnr.A2950

Chaichana, K. L., Kosztowski, T., Niranjan, A., Olivi, A., Weingart, J. D., Laterra, J., . . . Quinones-Hinojosa, A. (2010). Prognostic significance of contrast-enhancing anaplastic astrocytomas in adults. *J Neurosurg, 113*(2), 286-292. doi: 10.3171/2010.2.JNS091010

Cohen, J. (1960). A Coefficient of Agreement for Nominal Scales. *Educational and Psychological Measurement, 20*(1), 37-46. doi: 10.1177/001316446002000104

Colman, H., Zhang, L., Sulman, E. P., McDonald, J. M., Shooshtari, N. L., Rivera, A., . . . Aldape, K. (2010). A multigene predictor of outcome in glioblastoma. *Neuro Oncol, 12*(1), 49-57. doi: 10.1093/neuonc/nop007

Cooper, L. A., Kong, J., Gutman, D. A., Wang, F., Gao, J., Appin, C., . . . Saltz, J. H. (2012). Integrated morphologic analysis for the identification and characterization of disease subtypes. *J Am Med Inform Assoc, 19*(2), 317-323. doi: 10.1136/amiajnl-2011-000700

Curran, W. J., Scott, C. B., Horton, J., Nelson, J. S., Weinstein, A. S., Fischbach, A. J., . . . Nelson, D. F. (1993). Recursive Partitioning Analysis of Prognostic Factors in Three Radiation Therapy Oncology Group Malignant Glioma Trials. *J Natl Cancer Inst, 85*(9), 704-710. doi: 10.1093/jnci/85.9.704

Denecker, G., Vercammen, D., Declercq, W., & Vandenabeele, P. (2001). Apoptotic and necrotic cell death induced by death domain receptors. *Cell Mol Life Sci, 58*(3), 356-370.

Diehn, M., Nardini, C., Wang, D. S., McGovern, S., Jayaraman, M., Liang, Y., . . . Kuo, M. D. (2008). Identification of noninvasive imaging surrogates for brain tumor gene-expression modules. *Proc Natl Acad Sci U S A, 105*(13), 5213-5218. doi: 10.1073/pnas.0801279105

Drabycz, S., Roldán, G., de Robles, P., Adler, D., McIntyre, J. B., Magliocco, A. M., . . . Mitchell, J. R. (2010). An analysis of image texture, tumor location, and MGMT promoter methylation in glioblastoma using magnetic resonance imaging. *Neuroimage, 49*(2), 1398-1405. doi: 10.1016/j.neuroimage.2009.09.049

Ekici, M. A., Bulut, T., Tucer, B., & Kurtsoy, A. (2011). Analysis of the mortality probability of preoperative MRI features in malignant astrocytomas. *Turk Neurosurg, 21*(3), 271-279. doi: 10.5137/1019-5149.JTN.3321-10.3

Ellingson, B. M., Cloughesy, T. F., Lai, A., Nghiemphu, P. L., Mischel, P. S., & Pope, W. B. (2011). Quantitative volumetric analysis of conventional MRI response in recurrent glioblastoma treated with bevacizumab. *Neuro Oncol, 13*(4), 401-409. doi: 10.1093/neuonc/noq206

Eoli, M., Menghi, F., Bruzzone, M. G., De Simone, T., Valletta, L., Pollo, B., . . . Finocchiaro, G. (2007). Methylation of O6-Methylguanine DNA Methyltransferase and Loss of Heterozygosity on 19q and/or 17p Are Overlapping Features of Secondary Glioblastomas with Prolonged Survival. *Clinical Cancer Research, 13*(9), 2606-2613. doi: 10.1158/1078-0432.ccr-06-2184

Esteller, M., Garcia-Foncillas, J., Andion, E., Goodman, S. N., Hidalgo, O. F., Vanaclocha, V., . . . Herman, J. G. (2000). Inactivation of the DNA-Repair Gene MGMT and the Clinical Response of Gliomas to Alkylating Agents. *New England Journal of Medicine, 343*(19), 1350-1354. doi: 10.1056/NEJM200011093431901

Fisher, E. R., Palekar, A. S., Gregorio, R. M., Redmond, C., & Fisher, B. (1978). Pathological findings from the national surgical adjuvant breast project (Protocol No. 4). IV. Significance of tumor necrosis. *Hum Pathol, 9*(5), 523-530.

Frank, I., Blute, M. L., Cheville, J. C., Lohse, C. M., Weaver, A. L., & Zincke, H. (2002). An Outcome Prediction Model for Patients with Clear Cell Renal Cell Carcinoma Treated with Radical Nephrectomy Based on Tumor Stage, Size, Grade and Necrosis: The Ssign Score. *The Journal of Urology, 168*(6), 2395-2400. doi: 10.1016/s0022-5347(05)64153-5

Garzon, B., Emblem, K. E., Mouridsen, K., Nedregaard, B., Due-Tonnessen, P., Nome, T., . . . Kvinnsland, Y. (2011). Multiparametric analysis of magnetic resonance images for glioma grading and patient survival time prediction. *Acta Radiol, 52*(9), 1052-1060. doi: 10.1258/ar.2011.100510

George, A., Marquis-Nicholson, R., Zhang, L. T., Love, J. M., Ashton, F., Aftimos, S., . . . Love, D. R. (2011). Chromosome microarray analysis in a clinical environment: new perspective and new challenge. *Br J Biomed Sci, 68*(2), 100-108.

Grasbon-Frodl, E. M., Kreth, F. W., Ruiter, M., Schnell, O., Bise, K., Felsberg, J., . . . Kretzschmar, H. A. (2007). Intratumoral homogeneity of MGMT promoter hypermethylation as demonstrated in serial stereotactic specimens from anaplastic astrocytomas and glioblastomas. *Int J Cancer, 121*(11), 2458-2464. doi: 10.1002/ijc.23020

Hammoud, M. A., Sawaya, R., Shi, W., Thall, P. F., & Leeds, N. E. (1996). Prognostic significance of preoperative MRI scans in glioblastoma multiforme. *J Neurooncol, 27*(1), 65-73.

Hegi, M. E., Diserens, A.-C., Gorlia, T., Hamou, M.-F., de Tribolet, N., Weller, M., . . . Stupp, R. (2005). MGMT Gene Silencing and Benefit from Temozolomide in Glioblastoma. *New England Journal of Medicine, 352*(10), 997-1003. doi:10.1056/NEJMoa043331

Hobbs, S. K., Shi, G., Homer, R., Harsh, G., Atlas, S. W., & Bednarski, M. D. (2003). Magnetic resonance image-guided proteomics of human glioblastoma multiforme. *J Magn Reson Imaging, 18*(5), 530-536. doi: 10.1002/jmri.10395

Iliadis, G., Kotoula, V., Chatzisotiriou, A., Televantou, D., Eleftheraki, A. G., Lambaki, S., . . . Fountzilas, G. (2012). Volumetric and MGMT parameters in glioblastoma patients: survival analysis. *BMC Cancer, 12*, 3. doi: 10.1186/1471-2407-12-3

Kelly, P. J., Daumas-Duport, C., Kispert, D. B., Kall, B. A., Scheithauer, B. W., & Illig, J. J. (1987). Imaging-based stereotaxic serial biopsies in untreated intracranial glial neoplasms. *Journal of Neurosurgery, 66*(6), 865-874. doi:10.3171/jns.1987.66.6.0865

Kim, D. K., Alvarado, C. S., Abramowsky, C. R., Gu, L., Zhou, M., Soe, M. M., . . . Findley, H. W. (2005). Expression of inhibitor-of-apoptosis protein (IAP) livin by neuroblastoma cells: correlation with prognostic factors and outcome. *Pediatr Dev Pathol, 8*(6), 621-629. doi: 10.1007/s10024-005-4108-3

Krex, D., Klink, B., Hartmann, C., von Deimling, A., Pietsch, T., Simon, M., . . . Schackert, G. (2007). Long-term survival with glioblastoma multiforme. *Brain, 130*(Pt 10), 2596-2606. doi: 10.1093/brain/awm204

Kyritsis, A. P., Bondy, M. L., Xiao, M., Berman, E. L., Cunningham, J. E., Lee, P. S., . . . Saya, H. (1994). Germline p53 gene mutations in subsets of glioma patients. *J Natl Cancer Inst, 86*(5), 344-349.

Lacroix, M., Abi-Said, D., Fourney, D. R., Gokaslan, Z. L., Shi, W., DeMonte, F., . . . Sawaya, R. (2001). A multivariate analysis of 416 patients with glioblastoma multiforme: prognosis, extent of resection, and survival. *Journal of Neurosurgery, 95*(2), 190-198. doi: doi:10.3171/jns.2001.95.2.0190

Landis, J. R., & Koch, G. G. (1977). The Measurement of Observer Agreement for Categorical Data. *Biometrics, 33*(1), 159-174.

Lemasters, J. J. (1999). V. Necrapoptosis and the mitochondrial permeability transition: shared pathways to necrosis and apoptosis. *Am J Physiol, 276*(1 Pt 1), G1-6.

Liang, Y., Diehn, M., Watson, N., Bollen, A. W., Aldape, K. D., Nicholas, M. K., . . . Israel, M. A. (2005). Gene expression profiling reveals molecularly and clinically distinct subtypes of glioblastoma multiforme. *Proc Natl Acad Sci U S A, 102*(16), 5814-5819. doi: 10.1073/pnas.0402870102

Liu, Y., Cox, S. R., Morita, T., & Kourembanas, S. (1995). Hypoxia regulates vascular endothelial growth factor gene expression in endothelial cells. Identification of a 5' enhancer. *Circ Res, 77*(3), 638-643.

Lou, J. J. W., Chua, Y. L., Chew, E. H., Gao, J., Bushell, M., & Hagen, T. (2010). Inhibition of Hypoxia-Inducible Factor-1α (HIF-1α) Protein Synthesis by DNA Damage Inducing Agents. *PLoS One, 5*(5), e10522. doi: 10.1371/journal.pone.0010522

Louis, D. N., Ohgaki, H., Wiestler, O. D., Cavenee, W. K., Burger, P. C., Jouvet, A., . . . Kleihues, P. (2007). The 2007 WHO classification of tumours of the central nervous system. *Acta Neuropathol, 114*(2), 97-109. doi: 10.1007/s00401-007-0243-4

Ma, X., Lv, Y., Liu, J., Wang, D., Huang, Q., Wang, X., . . . Li, X. (2009). Survival analysis of 205 patients with glioblastoma multiforme: clinical characteristics, treatment and prognosis in China. *J Clin Neurosci, 16*(12), 1595-1598. doi: 10.1016/j.jocn.2009.02.036

Macdonald, D. R., Cascino, T. L., Schold, S. C., & Cairncross, J. G. (1990). Response criteria for phase II studies of supratentorial malignant glioma. *Journal of Clinical Oncology, 8*(7), 1277-1280.

Maher, E. A., Furnari, F. B., Bachoo, R. M., Rowitch, D. H., Louis, D. N., Cavenee, W. K., & DePinho, R. A. (2001). Malignant glioma: genetics and biology of a grave matter. *Genes & Development, 15*(11), 1311-1333. doi: 10.1101/gad.891601

Mao, H., LeBrun, D. G., Yang, J., Zhu, V. F., & Li, M. (2012). Deregulated Signaling Pathways in Glioblastoma Multiforme: Molecular Mechanisms and Therapeutic Targets. *Cancer Investigation, 30*(1), 48-56. doi:10.3109/07357907.2011.630050

Najafi, M., Soltanian-Zadeh, H., Jafari-Khouzani, K., Scarpace, L., & Mikkelsen, T. (2012). Prediction of Glioblastoma Multiform Response to Bevacizumab Treatment Using Multi-Parametric MRI. *PLoS One, 7*(1), e29945. doi: 10.1371/journal.pone.0029945

Norden, A. D., Young, G. S., Setayesh, K., Muzikansky, A., Klufas, R., Ross, G. L., . . . Wen, P. Y. (2008). Bevacizumab for recurrent malignant gliomas: efficacy, toxicity, and patterns of recurrence. *Neurology, 70*(10), 779-787. doi: 10.1212/01.wnl.0000304121.57857.38

Onoyama, Y., Abe, M., Yabumoto, E., Sakamoto, T., & Nishidai, T. (1976). Radiation therapy in the treatment of glioblastoma. *American Journal of Roentgenology, 126*(3), 481-492.

Park, J. K., Hodges, T., Arko, L., Shen, M., Dello Iacono, D., McNabb, A., . . . Black, P. M. (2010). Scale to Predict Survival After Surgery for Recurrent Glioblastoma Multiforme. *Journal of Clinical Oncology, 28*(24), 3838-3843. doi: 10.1200/jco.2010.30.0582

Pavlisa, G., Rados, M., Pavlisa, G., Pavic, L., Potocki, K., & Mayer, D. (2009). The differences of water diffusion between brain tissue infiltrated by tumor and peritumoral vasogenic edema. *Clinical Imaging, 33*(2), 96-101. doi: 10.1016/j.clinimag.2008.06.035

Pierallini, A., Bonamini, M., Osti, M., Pantano, P., Palmeggiani, F., Santoro, A., . . . Bozzao, L. (1996). Supratentorial glioblastoma: Neuroradiological findings and survival after surgery and radiotherapy. *Neuroradiology, 38*(0), S26-S30. doi: 10.1007/bf02278114

Pope, W. B., Chen, J. H., Dong, J., Carlson, M. R., Perlina, A., Cloughesy, T. F., . . . Nelson, S. F. (2008). Relationship between gene expression and enhancement in glioblastoma multiforme: exploratory DNA microarray analysis. *Radiology, 249*(1), 268-277. doi: 10.1148/radiol.2491072000

Pope, W. B., Lai, A., Nghiemphu, P., Mischel, P., & Cloughesy, T. F. (2006). MRI in patients with high-grade gliomas treated with bevacizumab and chemotherapy. *Neurology, 66*(8), 1258-1260. doi: 10.1212/01.wnl.0000208958.29600.87

Pope, W. B., Sayre, J., Perlina, A., Villablanca, J. P., Mischel, P. S., & Cloughesy, T. F. (2005). MR imaging correlates of survival in patients with high-grade gliomas. *AJNR Am J Neuroradiol, 26*(10), 2466-2474.

Prastawa, M., Bullitt, E., & Gerig, G. (2005). Synthetic ground truth for validation of brain tumor MRI segmentation. *Med Image Comput Comput Assist Interv, 8*(Pt 1), 26-33.

Quant, E. C., & Wen, P. Y. (2010). Novel medical therapeutics in glioblastomas, including targeted molecular therapies, current and future clinical trials. *Neuroimaging Clin N Am, 20*(3), 425-448. doi: 10.1016/j.nic.2010.04.007

Raza, S. M., Fuller, G. N., Rhee, C. H., Huang, S., Hess, K., Zhang, W., & Sawaya, R. (2004). Identification of Necrosis-Associated Genes in Glioblastoma by cDNA Microarray Analysis. *Clinical Cancer Research, 10*(1), 212-221. doi: 10.1158/1078-0432.ccr-0155-3

Rees, J. H., Smirniotopoulos, J. G., Jones, R. V., & Wong, K. (1996). Glioblastoma multiforme: radiologic-pathologic correlation. *Radiographics, 16*(6), 1413-1438; quiz 1462-1413.

Saraswathy, S., Crawford, F. W., Lamborn, K. R., Pirzkall, A., Chang, S., Cha, S., & Nelson, S. J. (2009). Evaluation of MR markers that predict survival in patients with newly

diagnosed GBM prior to adjuvant therapy. *J Neurooncol, 91*(1), 69-81. doi: 10.1007/s11060-008-9685-3

Shirai, K., Siedow, M. R., & Chakravarti, A. (2012). Antiangiogenic therapy for patients with recurrent and newly diagnosed malignant gliomas. *J Oncol, 2012*, 193436. doi: 10.1155/2012/193436

Soltanian-Zadeh, H., Windham, J. P., Peck, D. J., & Mikkelsen, T. (1998). Feature space analysis of MRI. *Magn Reson Med, 40*(3), 443-453.

Stieber, V. W., & Mehta, M. P. (2007). Advances in radiation therapy for brain tumors. *Neurol Clin, 25*(4), 1005-1033, ix. doi: 10.1016/j.ncl.2007.07.005

Strand, C., Enell, J., Hedenfalk, I., & Ferno, M. (2007). RNA quality in frozen breast cancer samples and the influence on gene expression analysis--a comparison of three evaluation methods using microcapillary electrophoresis traces. *BMC Mol Biol, 8*, 38. doi: 10.1186/1471-2199-8-38

Stupp, R., Mason, W. P., van den Bent, M. J., Weller, M., Fisher, B., Taphoorn, M. J. B., . . . Mirimanoff, R. O. (2005). Radiotherapy plus Concomitant and Adjuvant Temozolomide for Glioblastoma. *New England Journal of Medicine, 352*(10), 987-996. doi: doi:10.1056/NEJMoa043330

Swinson, D. E. B., Jones, J. L., Richardson, D., Cox, G., Edwards, J. G., & O'Byrne, K. J. (2002). Tumour necrosis is an independent prognostic marker in non-small cell lung cancer: correlation with biological variables. *Lung Cancer, 37*(3), 235-240. doi: 10.1016/s0169-5002(02)00172-1

Therasse, P., Arbuck, S. G., Eisenhauer, E. A., Wanders, J., Kaplan, R. S., Rubinstein, L., . . . Gwyther, S. G. (2000). New Guidelines to Evaluate the Response to Treatment in Solid Tumors. *J Natl Cancer Inst, 92*(3), 205-216. doi: 10.1093/jnci/92.3.205

Tonn, J. C., & Stummer, W. (2008). Fluorescence-guided resection of malignant gliomas using 5-aminolevulinic acid: practical use, risks, and pitfalls. *Clin Neurosurg, 55*, 20-26.

Tugcu, B., Postalci, L. S., Gunaldi, O., Tanriverdi, O., & Akdemir, H. (2010). Efficacy of clinical prognostic factors on survival in patients with glioblastoma. *Turk Neurosurg, 20*(2), 117-125. doi: 10.5137/1019-5149.JTN.2461-09.4

Tusher, V. G., Tibshirani, R., & Chu, G. (2001). Significance analysis of microarrays applied to the ionizing radiation response. *Proc Natl Acad Sci U S A, 98*(9), 5116-5121. doi: 10.1073/pnas.091062498

Van Meir, E. G., Hadjipanayis, C. G., Norden, A. D., Shu, H. K., Wen, P. Y., & Olson, J. J. (2010). Exciting new advances in neuro-oncology: the avenue to a cure for malignant glioma. *CA Cancer J Clin, 60*(3), 166-193. doi: 10.3322/caac.20069

Verhaak, R. G., Hoadley, K. A., Purdom, E., Wang, V., Qi, Y., Wilkerson, M. D., . . . Hayes, D. N. (2010). Integrated genomic analysis identifies clinically relevant subtypes of glioblastoma characterized by abnormalities in PDGFRA, IDH1, EGFR, and NF1. *Cancer Cell, 17*(1), 98-110. doi: 10.1016/j.ccr.2009.12.020

Vitucci, M., Hayes, D. N., & Miller, C. R. (2011). Gene expression profiling of gliomas: merging genomic and histopathological classification for personalised therapy.*Br J Cancer, 104*(4), 545-553. doi: 10.1038/sj.bjc.6606031

Vucic, D., Stennicke, H. R., Pisabarro, M. T., Salvesen, G. S., & Dixit, V. M. (2000). ML-IAP, a novel inhibitor of apoptosis that is preferentially expressed in human melanomas. *Curr Biol, 10*(21), 1359-1366.

Wang, H., Pan, K., Zhang, H. K., Weng, D. S., Zhou, J., Li, J. J., . . . Xia, J. C. (2008). Increased polycomb-group oncogene Bmi-1 expression correlates with poor prognosis in hepatocellular carcinoma. *J Cancer Res Clin Oncol, 134*(5), 535-541. doi: 10.1007/s00432-007-0316-8

Wang, M. Y., Cheng, J. L., Han, Y. H., Li, Y. L., Dai, J. P., & Shi, D. P. (2011). Measurement of tumor size in adult glioblastoma: Classical cross-sectional criteria on 2D MRI or volumetric criteria on high resolution 3D MRI? *Eur J Radiol*. doi: 10.1016/j.ejrad.2011.05.017

Westphal, M., Hilt, D. C., Bortey, E., Delavault, P., Olivares, R., Warnke, P. C., . . . Ram, Z. (2003). A phase 3 trial of local chemotherapy with biodegradable carmustine (BCNU) wafers (Gliadel wafers) in patients with primary malignant glioma. *Neuro Oncol, 5*(2), 79-88. doi: 10.1215/S1522-8517-02-00023-6

White, M. L., Zhang, Y., Kirby, P., & Ryken, T. C. (2005). Can Tumor Contrast Enhancement Be Used as a Criterion for Differentiating Tumor Grades of Oligodendrogliomas? *American Journal of Neuroradiology, 26*(4), 784-790.

Whittle, I. R., & Gregor, A. (1991). The treatment of primary malignant brain tumours. *J Neurol Neurosurg Psychiatry, 54*(2), 101-103.

Yamada, S., Takai, Y., Nemoto, K., Ogawa, Y., Kakuto, Y., Hoshi, A., . . . Yoshimoto, T. (1992). Radioresponse and prognosis of malignant glioma. *Tohoku J Exp Med, 167*(1), 79-87.

Zagzag, D., Goldenberg, M., & Brem, S. (1989). Angiogenesis and blood-brain barrier breakdown modulate CT contrast enhancement: an experimental study in a rabbit brain-tumor model. *AJR Am J Roentgenol, 153*(1), 141-146.

Zinn, P. O., Majadan, B., Sathyan, P., Singh, S. K., Majumder, S., Jolesz, F. A., & Colen, R. R. (2011). Radiogenomic Mapping of Edema/Cellular Invasion MRI-Phenotypes in Glioblastoma Multiforme. *PLoS One, 6*(10), e25451. doi: 10.1371/journal.pone.0025451

Imaging Feature	Proposed prognostic value on overall survival	Source
Contrast Enhancement	--	(Pierallini et al., 1996)
	++	(Ma et al., 2009)
	++	(Hammoud et al., 1996)
	++	(Chaichana et al., 2010)
Necrotic Volume	--	(Pope et al., 2005)
	++	(Pierallini et al., 1996)
	++	(Barker et al., 1996)
	++	(Lacroix et al., 2001)
	++	(Ekici et al., 2011)
Edema Volume	--	(Pierallini et al., 1996)
	--	(Ekici et al., 2011)
	++	(Pope et al., 2005)
	++	(Hammoud et al., 1996)
Total Tumor Volume	--	(Pope et al., 2005)
	--	(Pierallini et al., 1996)
	--	(Hammoud et al., 1996)
	++	(Iliadis et al., 2012)
Total Abnormality Volume	--	(Iliadis et al., 2012)
Total Abnormal Volume / Total Tumor	++	(Ellingson et al., 2011)*
Tumor Location	--	(Hammoud et al., 1996)
	++	(Onoyama, Abe, Yabumoto, Sakamoto, & Nishidai, 1976)

Table 1: Summary of studies implicating MRI features of GBMs with overall survival. Note all studies above used categorical estimates of image features. ++ Indicates that the feature was found to be significantly associated with survival. -- Indicates that no significant association with survival was found. * Indicates bevacizumab chemotherapy

Image Feature	Number of Patients	Mean (cm^3)	Skewness	Standard Deviation (cm^3)
Necrotic Volume	89	22.203	0.8514	15.078
Edema Volume	89	63.059	0.7371	44.064
Contrast Enhancing Volume	89	17.931	1.156	13.045
Total Tumor Volume	89	40.134	0.9385	27.625
Total Abnormal Volume	89	103.194	0.5266	55.378

Table 2: Descriptive statistics for several imaging features. Total Tumor volume refers to the combination of necrotic and contrast enhancing volumes. Total Abnormal Volume consists of the combination of total tumor and edema volumes.

A

Variable	Hazard Ratio (HR)	95% Confidence Interval	P Value
Gender	1.115	0.854 - 1.376	0.684
KPS	1.473	0.941 - 2.005	**0.046**
Age	1.015	0.699 - 1.331	0.124
Necrosis (mm3)	1.365	0.986 - 1.89	0.061
Contrast Enhancement (mm3)	1.276	0.929 - 1.752	0.132
Edema (mm3)	0.766	0.569 - 1.031	0.078
Total Abnormal (mm3)	1.028	0.698 - 1.516	0.887
Total Tumor (mm3)	1.339	0.963 - 1.863	0.083
Necrosis / Edema	**1.578**	**1.207 - 2.063**	**0.001**
Necrosis / Total Tumor	2.932	0.515 - 16.685	0.225
Percent Necrosis	**1.862**	**1.163 - 2.982**	**0.01**
Contrast Enhancement / Edema	**0.658**	**0.497 - 0.871**	**0.003**
Contrast Enhancement / Total Tumor	0.481	0.119 - 1.947	0.305
Percent Contrast Enhancement	1.585	0.997 - 2.519	0.052
Percent Edema	**0.353**	**0.213 - 0.585**	**<0.001**
Total Tumor / Edema	**1.837**	**1.116 - 3.026**	**0.017**
Contrast Enhancement / Necrosis	0.64	0.294 - 1.394	0.262
Total Tumor / Total Abnormality	**1.817**	**1.108 - 2.978**	**0.018**
Abs(Necrosis – Contrast Enhancement	1.306	0.954 - 1.658	0.051
Abs(Total Abnormal – Total Tumor)	0.766	0.503 - 1.029	0.078

B

Variable	Hazard Ratio (HR)	95% Confidence Interval	P Value
KPS	1.287	0.869 - 1.906	0.208
Percent Necrosis	**1.713**	**1.053 - 2.787**	**0.03**

Table 3: Cox proportional hazards model univariate (A) and multivariate (B) analyses of individual parameters for correlations with overall survival rate. KPS: Karnofsky Performance Scale score (see Introduction). Significant values ($P<0.05$) are indicated in bold.

Imaging Feature	T statistic	Degrees of Freedom	Significance (2-tailed)
Edema (mm^3)	1.266	83	.209
Necrosis (mm^3)	1.058	83	.293
Contrast Enhancement (mm^3)	.860	83	.392
Total Tumor (mm^3)	.985	83	.328
Total Abnormality (mm^3)	1.475	83	.144
Percent Contrast Enhancement	-.839	83	.404
Percent Necrosis	-.828	83	.410
Percent Edema	.865	83	.390
Necrosis / Edema	-1.103	17.431	.285*
Contrast Enhancement / Total Abnormality	.445	83	.657
Contrast Enhancement / Edema	-1.050	18.563	.307*
Total Tumor / Edema	-1.085	17.882	.292*
Contrast Enhancement / Necrosis	.129	83	.898
Necrosis / Total Tumor	-.445	83	.657
Total Tumor / Total Abnormality	-.865	83	.390
Abs (Contrast Enhancement – Necrosis)	.361	83	.719
Edema / Total Tumor	.921	83	.360

Table 4: Comparisons of 17 individual imaging feature measurements between patients with or without TP53 mutations. No features showed significant difference between mutation statuses. All t tests assume equal variance unless indicated by *

Imaging Feature	T statistic	Degrees of Freedom	Significance (2-tailed)
Edema (mm3)	-.390	83	.698
Necrosis (mm3)	.172	83	.864
Contrast Enhancement (mm3)	.521	83	.604
Total Tumor (mm3)	.340	83	.735
Total Abnormality (mm3)	-.140	83	.889
Percent Contrast Enhancement	1.193	83	.236
Percent Necrosis	.466	83	.643
Percent Edema	-.834	83	.407
Necrosis / Edema	.858	83	.393
Contrast Enhancement / Total Tumor	1.138	83	.258
Contrast Enhancement / Edema	.925	83	.358
Total Tumor / Edema	.898	83	.372
Contrast Enhancement / Necrosis	1.242	83	.218
Necrosis / Total Tumor	-1.138	83	.258
Total Tumor / Total Abnormality	.834	83	.407
Abs (Contrast Enhancement / Necrosis)	.060	83	.952
Edema / Total Tumor	.191	29.685	.849*

Table 5: Comparisons of 17 individual imaging feature measurements between patients with or without EGFR mutations. No features showed significant difference between mutation statuses. All t tests assume equal variance unless indicated by *

Imaging Feature	t statistic	Degrees of Freedom	Significance (2-tailed)
Edema in mm3	.297	49	.768
Necrosis in mm3	.431	49	.668
Contrast Enhancement in mm3	-.055	49	.956
Total tumor ball Volume in mm3	.196	49	.846
Total everything - FLAIR volume in mm3	.319	49	.751
Percent Contrast Enhancement	-1.605	49	.115
Percent Necrosis	-.630	49	.532
Percent Edema	1.153	49	.255
necrosis/edema	-.821	49	.416
Contrast Enhancement / Total Tumor	-2.932	49	**.005**
Contrast Enhancement / Edema	-.759	49	.452
Total Tumor / Edema	-.790	49	.434
Contrast Enhancement / Necrosis	-2.969	49	**.005**
Necrosis / Total Tumor	2.932	49	**.005**
Total Tumor / Total Abnormality	-1.153	49	.255
Abs (Contrast Enhancement / Necrosis)	1.423	49	.161
Edema / Total Tumor	.571	49	.571

Table 6: Comparisons of 17 individual imaging feature measurements between patients with or without MGMT promoter hypermethylation. Significant features are indicated in bold. All t tests assume equal variance unless indicated by *

Imaging Feature		df	F	Sig.
Total Tumor / Edema	Between Groups	3	.979	.407
	Within Groups	81		
Abs (Necrosis – Contrast enhancement)	Between Groups	3	1.213	.310
	Within Groups	81		
Total Tumor / Total Abnormality	Between Groups	3	.371	.774
	Within Groups	81		
Necrosis / Total Tumor	Between Groups	3	.914	.438
	Within Groups	81		
Contrast Enhancement / Necrosis	Between Groups	3	1.281	.287
	Within Groups	81		
Total Tumor / Edema	Between Groups	3	.797	.499
	Within Groups	81		
Contrast Enhancement / Edema	Between Groups	3	.951	.420
	Within Groups	81		
Contrast Enhancement / Total Tumor	Between Groups	3	.914	.438
	Within Groups	81		
Necrosis / Edema	Between Groups	3	.667	.575
	Within Groups	81		
Percent Edema	Between Groups	3	.371	.774
	Within Groups	81		
Percent Necrosis	Between Groups	3	.097	.961
	Within Groups	81		
Percent Contrast Enhancement	Between Groups	3	.824	.485
	Within Groups	81		
Total Abnormality (mm^3)	Between Groups	3	.458	.713
	Within Groups	81		
Total Tumor (mm^3)	Between Groups	3	.572	.635
	Within Groups	81		
Contrast Enhancement (mm^3)	Between Groups	3	.767	.516
	Within Groups	81		
Necrosis in (mm^3)	Between Groups	3	.433	.730
	Within Groups	81		
Edema in (mm^3)	Between Groups	3	.275	.843
	Within Groups	81		

Table 7: Analysis of Variance (ANOVA) of individual features among the four molecular subtypes of GBM. None of the imaging features showed significant difference between molecular subtypes.

Pathway	P-value	Gene Symbol	Gene Name
Hypoxia-Inducible Factor Signaling	0.0000643	EIF2B3	Eukaryotic translation initiation factor 2B, subunit 3
		EIF2B4	Eukaryotic translation initiation factor 2B, subunit 4
		EIF2B5	Eukaryotic translation initiation factor 2B, subunit 5
		SUMO1	SMT3 suppressor of mif two 3 homolog 1
		UBE2I	Ubiquitin-conjugating enzyme E2I
Anti-Apoptosis	0.0159	BIRC7	Baculoviral IAP repeat containing 7
		BNIP1	BCL2/adenovirus E1B 19kDa interacting protein 1
Cell Cycle: G2/M DNA Damage Checkpoint Regulation	0.0341	CKS2	CDC28 protein kinase regulatory subunit 2
		MYT1	Myelin transcription factor
Mitochondrial Dysfunction	0.0501	NDUFA2	NADH dehydrogenase (ubiquinone) 1 alpha subcomplex
		NDUFS5	NADH dehydrogenase (ubiquinone) Fe-S protein 5
		RHOT2	Ras homolog gene family, member T2

Table 8: Results of IPA functional analysis for the 118 genes correlated with percent necrosis and the respective levels of significance.

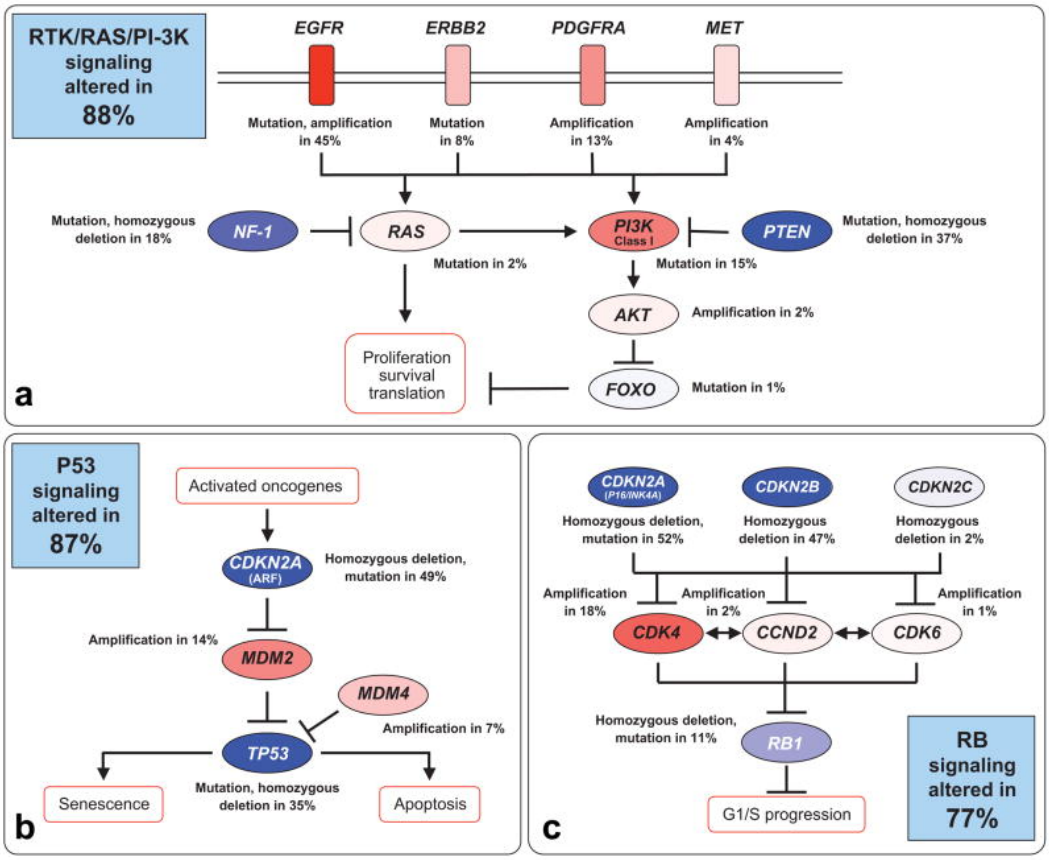

Figure 1: Three molecular signaling pathways in GBM. Copy number alteration and DNA mutation changes are indicated in the receptor tyrosine kinase (RTK), RAS, and phosphoinositol–3–kinase (PI3K) pathway (a); the p53 tumor suppressor pathway (b); and the retinoblastoma (Rb) tumor suppressor pathway (c). Shades of red indicate activating alterations while shades of blue indicate inactivating alterations. The frequency of various alterations across TCGA patients are indicated as percentages. Blue boxes indicate percentages of GBMs with alterations in at least one aspect of the indicated pathway. Reprinted with permission from The Cancer Genome Atlas Research Network. Comprehensive genomic characterization defines human glioblastoma genes and core pathways. *Nature*. 2008;455:1061–1068

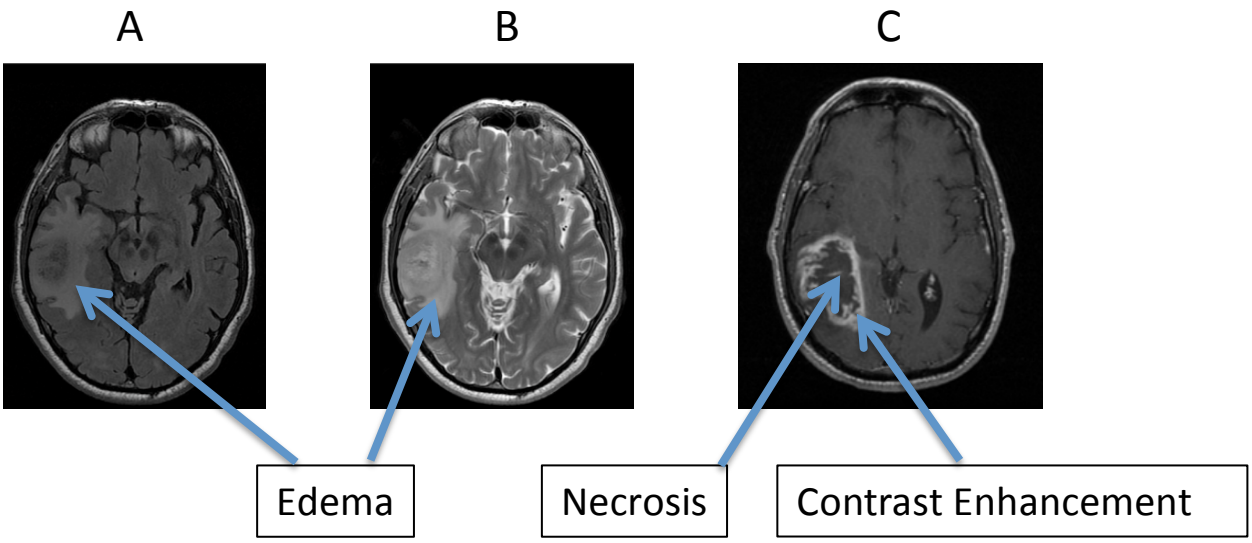

Figure 2: GBM visualized using different MRI sequences. FLAIR (A) and T2 weighted (B) images are ideally suited for visualizing edema whereas T1 weighted post Gd (C) images are best suited for visualizing necrosis (decreased signal intensity) and contrast enhancement (surrounding rim of increased signal intensity).

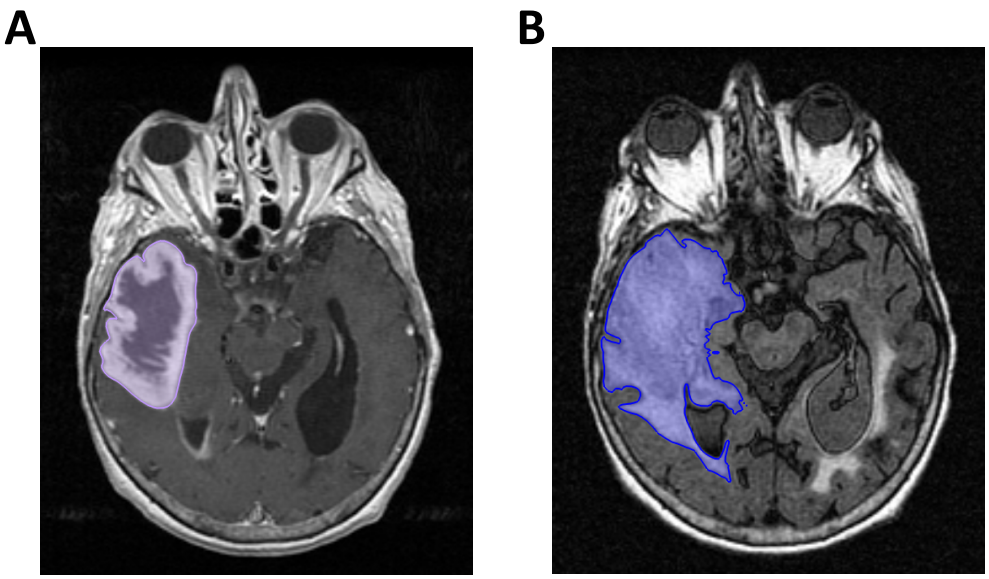

Figure 3: Binary mask segmentation for a 60 year old male patient with a right temporal GBM. Masks were manually drawn in Velocity A1 using the 2D flood fill tool (Purple, blue areas) to cover tumor volumes on (A) Post Gd images and (B) FLAIR images. Note that the FLAIR "envelope" includes both edema (hyper intense signal) as well as the tumor itself, minus the area occupied by the ventricles.

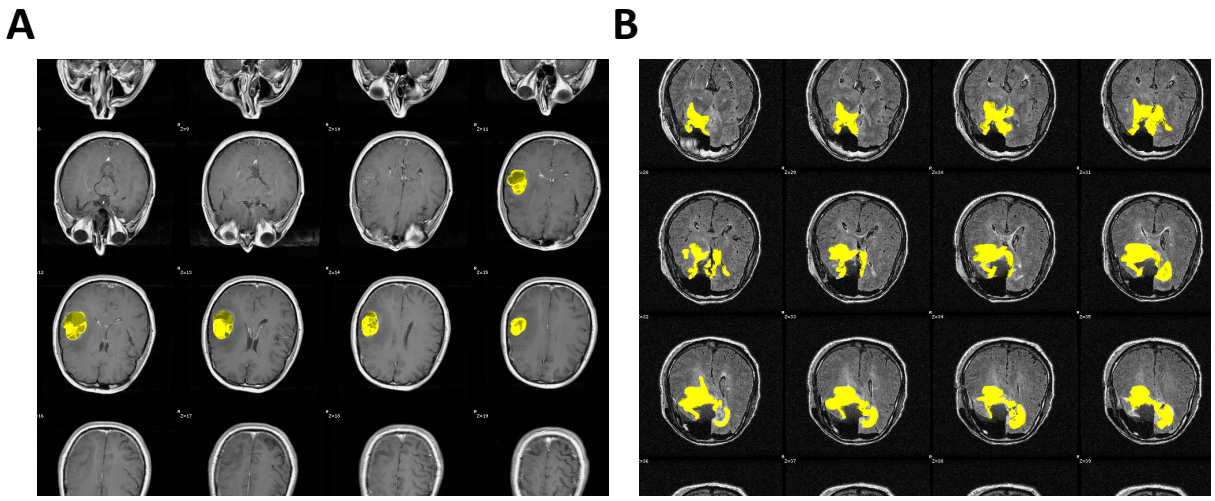

Figure 4: TumorView Dynamic Reader. Image sets of TCGA patients with accompanying binary masks were uploaded onto an ad hoc website and analyzed. Patients with acceptable images and mask overlay (A) were cleared for further analysis whereas patients with poor images or post-surgical images (B) were excluded.

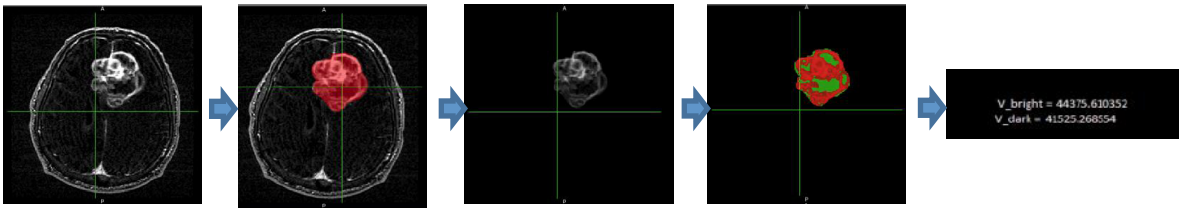

Figure 5: Semi-automated *in silico* segmentation and measurement method for T1 weighted post Gd images. Tumor volume is identified by a manually drawn binary mask (Red) in Velocity AI. K means clustering divides pixels covered by the mask into bright (red, contrast enhancement) and dark (green, necrosis) clusters based on relative pixel intensity. Volume of individual features can be estimated by converting voxels into mm^3.

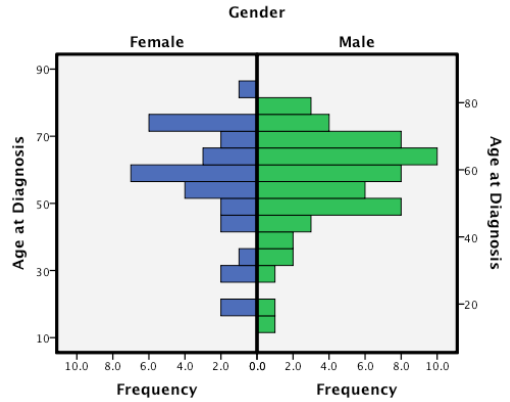

Figure 6: Patient Characteristics. 89 total patients with MRI sets amenable to necrosis, contrast enhancement, and edema image feature measurement were included in the study. 57 patients were male and the average age was 56.9 years old (Range: 14 to 84 yrs old).

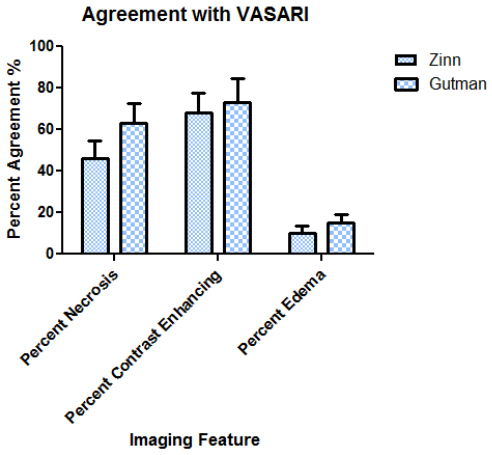

Figure 7: Percent agreement between measurements made by Gutman *et al*. (current study) and ratings by neuroradiologists according to VASARI standard. For comparison, measurements from Zinn *et al.* are plotted as well. Percent agreement to the Vasari standard within each imaging feature does not differ between our measures (Gutman *et al*.) and those made by Zinn *et al*. Error Bars represent 95% confidence intervals.

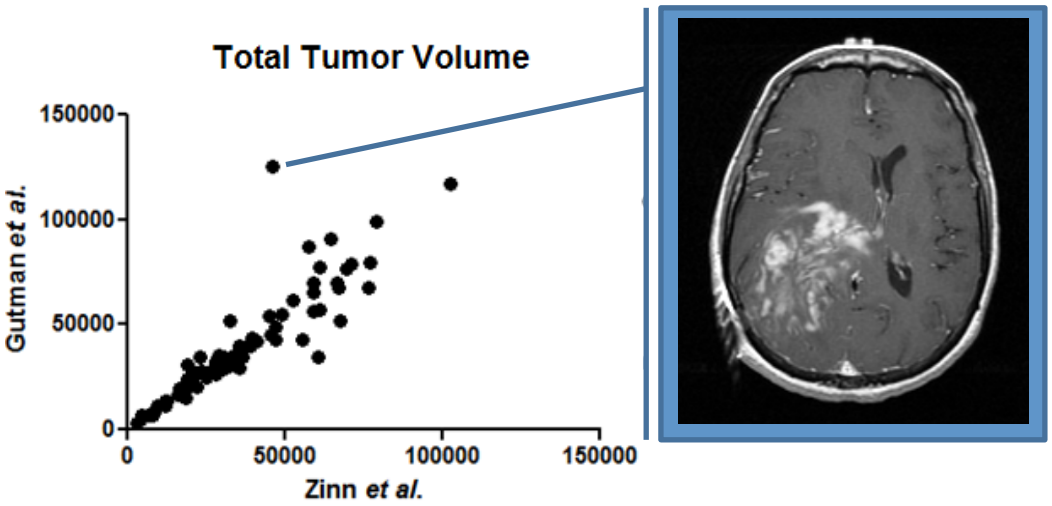

Figure 8: Correlations of total tumor measurements between Zinn *et al.* and Gutman *et al.* (left). Patient TCGA-06-0162 was removed from future analyses due to ambiguous contrast enhancement/necrosis regions and possible post-surgical scan (see skull) (right).

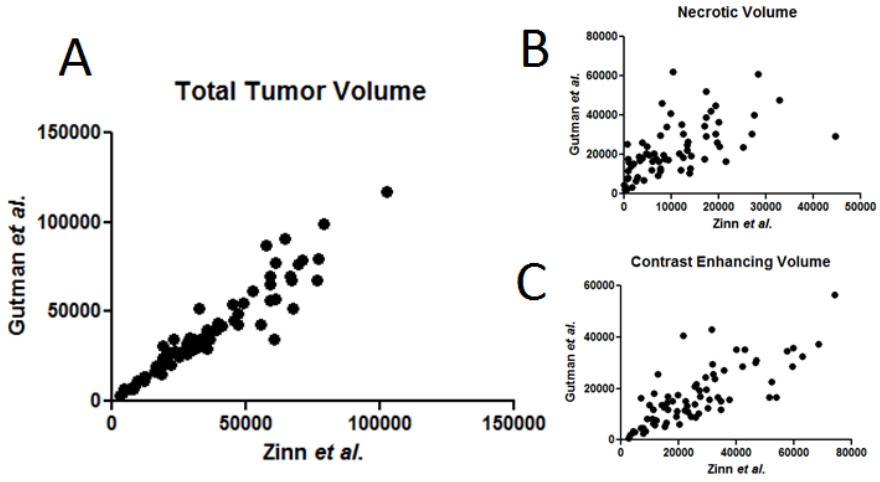

Figure 9: Correlations between total tumor volume (A), necrotic volume (B), and contrast enhancing volumes (C) measurements between measurements made by Zinn *et al.* and our measurements (Gutman *et al.*), without including patient TCGA-06-0162. A tighter correlation is observed for small volumes with more variability at large volumes. Correlations are also stronger in general for total tumor volume ($r(70)=0.944$, $p<0.0001$) than for necrotic volume ($r(70)=0.612$, $p<0.0001$) or contrast enhancement volume ($r(70)=0.770$, $p<0.0001$).

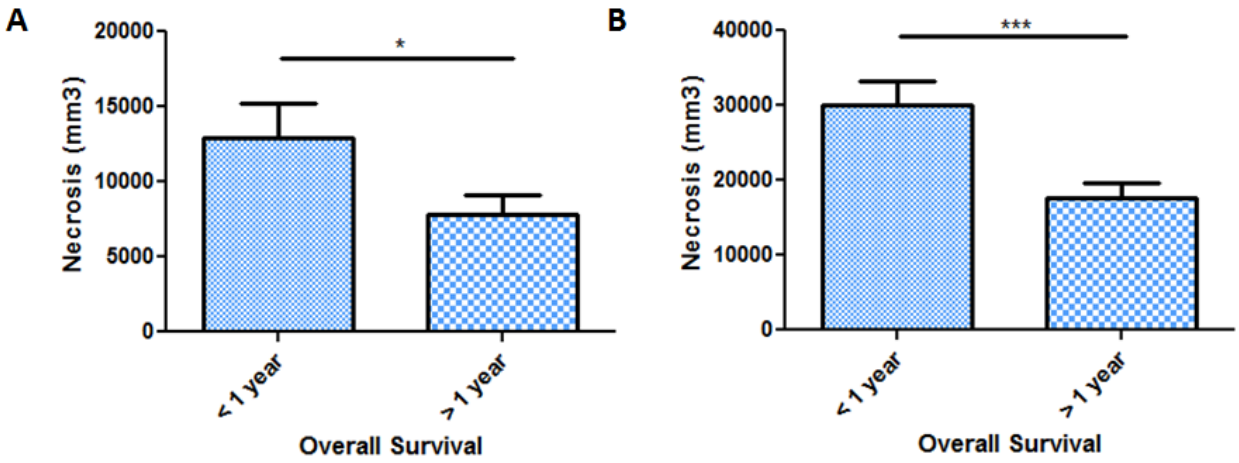

Figure 10: Comparison of the difference in the amount of necrosis between patients surviving less than a year and patients surviving more than a year based on the measurements from Zinn et al. (A) and the measurements from our methodology (B). Using this metric, our measurements show a higher significant difference between the two groups (P=0.0006 vs. P=0.0212).

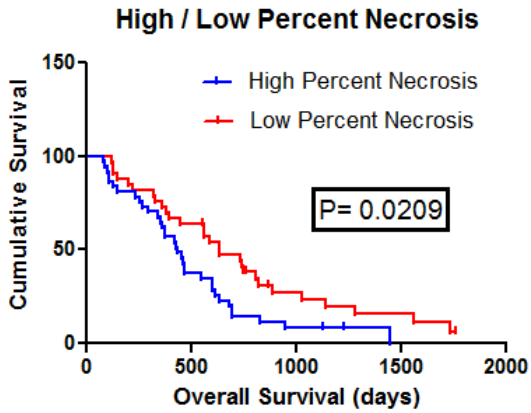

Figure 11: Kaplan-Meier survival analysis of patients with percent necrosis above the median (19.5%) and those with percent necrosis below the median ($n_{1,2} = 35$). Survival for patients with high percent necrosis was significantly lower than that for patients with low percent necrosis (log rank, p = 0.0209). Median survival was 557 days (low percent necrosis) vs. 370 days (high percent necrosis).

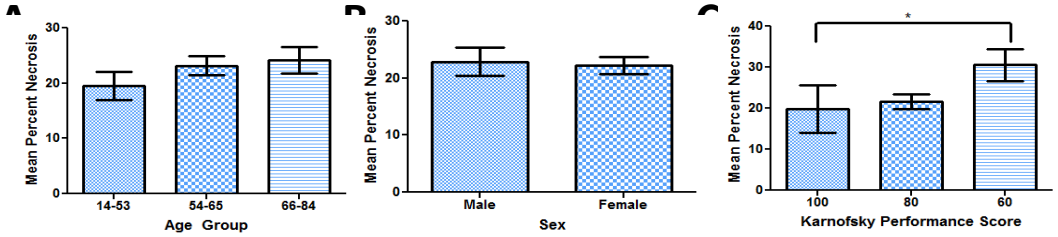

Fig 12: Distribution of percent necrosis across patient characteristics implicated in survival. Mean necrosis does not significantly differ between (A) age (F(2,86) = 1.133, 0.327) or (B) sex (t(87)=0.236, p = 0.814). Patients with KPS scores of 60 show significantly more necrosis than those with scores of 100 (Tukey's Post Hoc (p=0.043)).

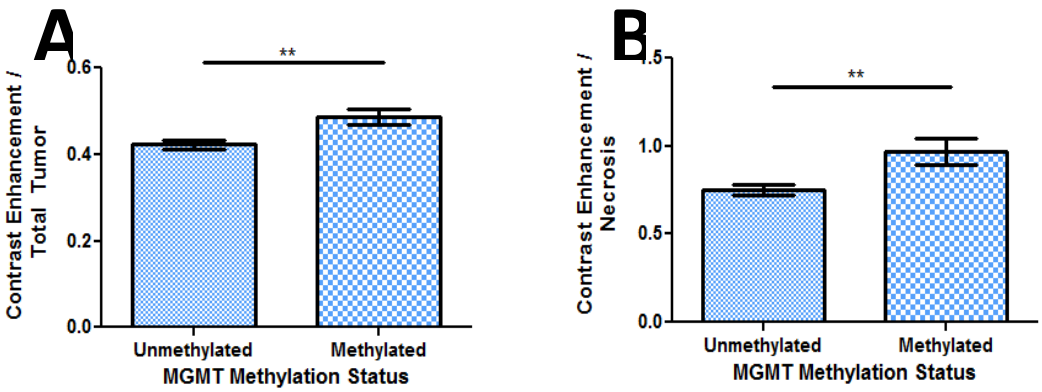

Figure 13: Effect of MGMT methylation on various imaging features. MGMT promoter methylation is associated with higher Contrast Enhancement / Total Tumor ratios (A) and Contrast Enhancement / Necrosis ratios (B).

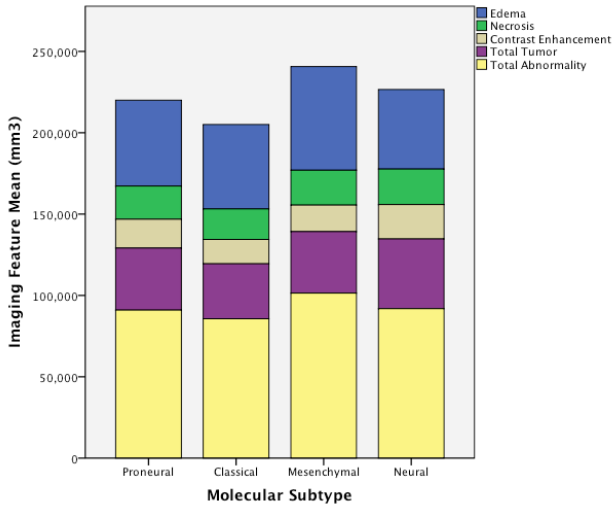

Figure 14: Mean volumes of Edema, Necrosis, Contrast Enhancement, Total Tumor, and Total Abnormality for each molecular subtype as defined by Verhaak *et a*l. Between subjects one way ANOVAs for each imaging feature grouped by molecular subtype showed no statistical significance for any imaging feature variable. See Table 7 for significance.

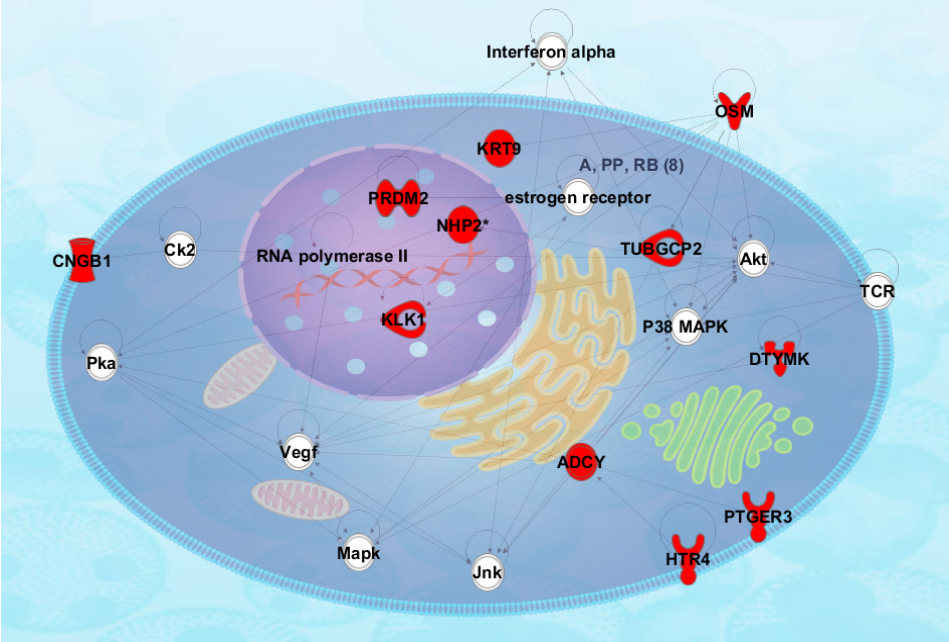

Figure 15: Representation of genes consistently expressed in tumors with high percent necrosis using IPA Pathway Builder. Genes up-regulated in high necrosis patients (Red) are involved in several pathways including cell-to-cell signaling and interaction, cellular growth and proliferation, and connective tissue development and function pathways (white). Dashed lines indicate experimentally determined indirect interactions. Complete lines indicate direct interactions.

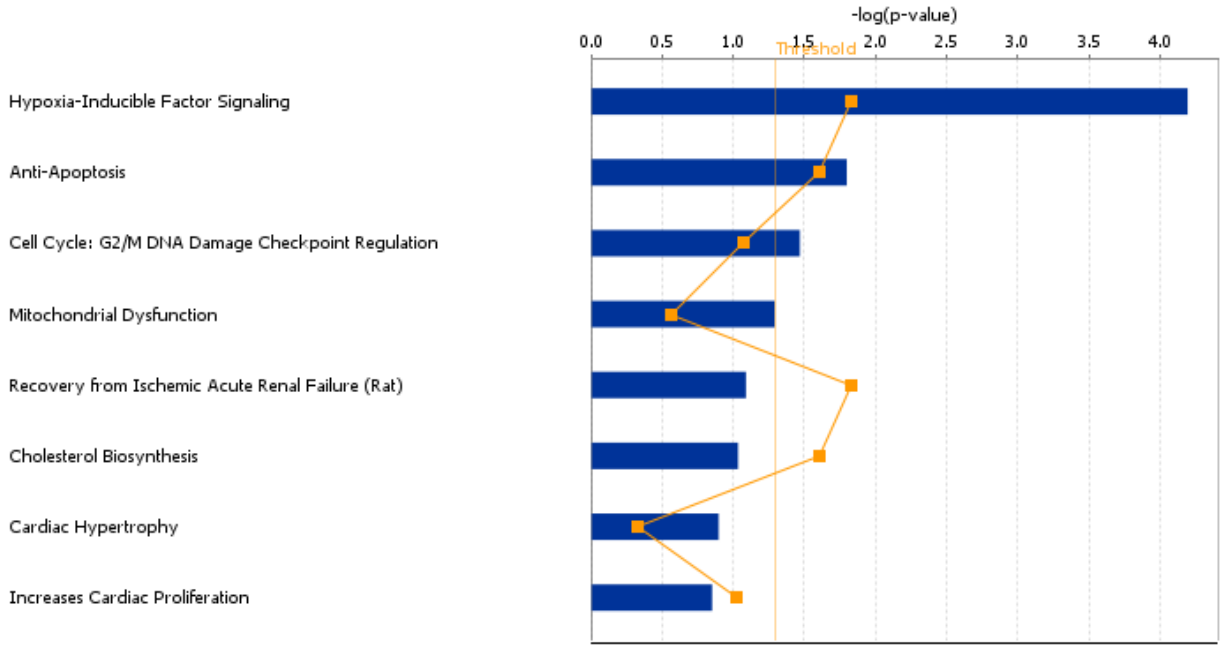

Figure 16: Results of IPA Functional analysis for 118 genes consistently correlated with percent necrosis. Significantly associated functions are represented by blue bars containing the orange threshold line.

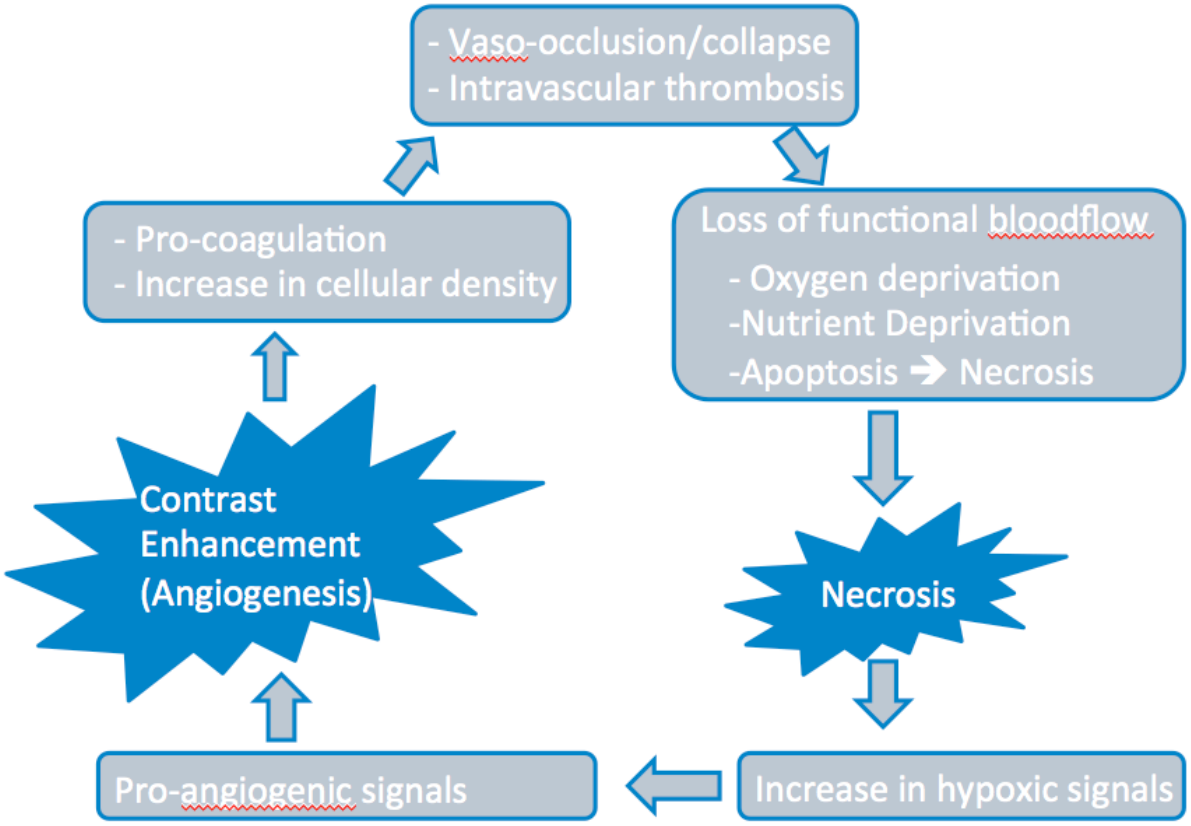

Figure 17: Schematic representation of a proposed relationship between contrast enhancement and necrosis. Growth signals and angiogenic signals increase tumor vasculature. The resulting increase in coagulation and cellular density starve the cells of oxygen and nutrients. The starved hypoxic state cause the production of more growth signals. See text for details.

[indeterminate, none (0%), <5%, 6-33%, 34-67%, 68-95%, >95%, All (100%)]. What proportion of the entire tumor is enhancing. (Assuming that the entire abnormality may be comprised of: (1) an enhancing component, (2) a non-enhancing component, (3) a necrotic component and (4) a edema component.)	0= - 1= n/a 2=None (0%) 3= <5% 4= 6-33% 5= 34-67% 6= 68-95% 7= >95% 8=All (100%) 9= Indeterminate

[indeterminate, none (0%), <5%, 6-33% , 34-67%, 68-95%, >95%, All (100%)]. (Necrosis is defined as a region within the tumor that does not enhance or shows markedly diminished enhancement, is high on T2W and proton density images, is low on T1W images, and has an irregular border). (Assuming that the the entire abnormality may be comprised of: (1) an enhancing component, (2) a non-enhancing component, (3) a necrotic component and (4) a edema component.)	0= - 1= n/a 2=None (0%) 3= <5% 4= 6-33% 5= 34-67% 6= 68-95% 7= >95% 8=All (100%) 9= Indeterminate

[indeterminate, none (0%), <5%, 6-33%, 34-67%, 68-95%, >95%, All (100%)]. What proportion of the entire abnormality is vasogenic edema? (Edema should be greater in signal than than nCET and somewhat lower in signal than CSF. Pseudopods are characteristic of edema). (Assuming that the the entire abnormality may be comprised of: (1) an enhancing component, (2) a non-enhancing component, (3) a necrotic component and (4) a edema component.)	0= - 1= n/a 2=None (0%) 3= <5% 4= 6-33% 5= 34-67% 6= 68-95% 7= >95% 8=All (100%) 9= Indeterminate

Appendix Figure 1: Subset of VASARI imaging guidelines used by neuroradiologists to classify brain tumors on MR scans. Note the categorical nature of the guidelines.

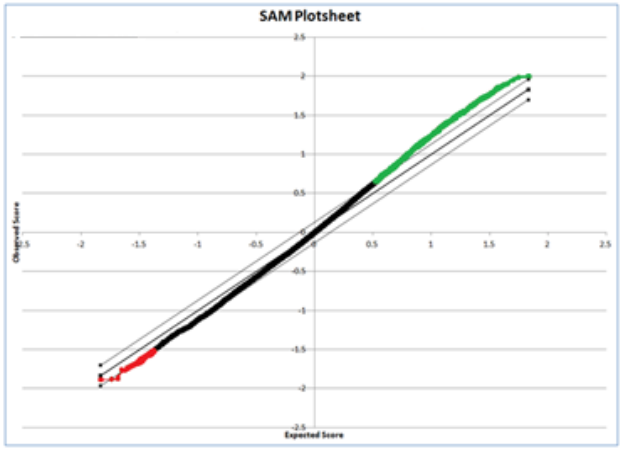

Appendix Figure 2: Graphical representation of the results of a two class non parametric Statistical Analysis of Microarray (SAM) analysis. Genes above upper FDR threshold are considered significantly up regulated in necrosis patients and are indicated in green. Red genes are inversely correlated to increasing levels of tumor necrosis.

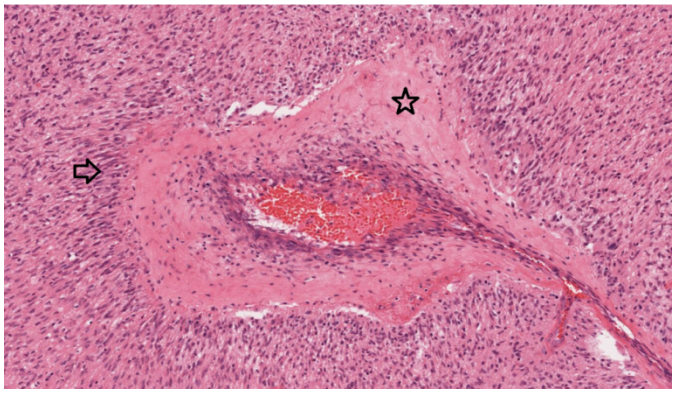

Appendix Figure 3: Area of necrosis surrounding an occluded blood vessel in a diagnostic histology slide for patient TCGA-02-0037, who had 56% necrosis visualized by his MRI scan. Arrowhead points to pseudopalisading necrosis migrating away from the central necrotic core, which is indicated by the star.

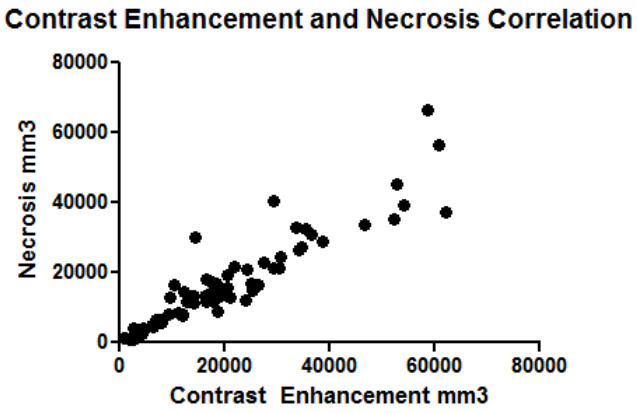

Appendix Figure 4: Correlation between amount of necrosis and contrast enhancement. Pearson $r(68) = 0.921$, $p < .0001$.